ACS APPLIED MATERIALS & INTERFACES

www.acsami.org

Forum Article

Controlled Release of the Anticancer Drug Cyclophosphamide from a Superparamagnetic β-Cyclodextrin Nanosponge by Local Hyperthermia Generated by an Alternating Magnetic Field

Sebastián Salazar Sandoval,*,¶ Patricia Díaz-Saldívar,¶ Ingrid Araya, Freddy Celis, Diego Cortés-Arriagada, Ana Riveros, Carlos Rojas-Romo, Carolina Jullian, Nataly Silva, Nicolás Yutronic, Marcelo J. Kogan,* and Paul Jara*

Cite This: https://doi.org/10.1021/acsami.3c18038

Read Online

ACCESS | Metrics & More | Article Recommendations

ABSTRACT: A β-cyclodextrin (β-CD) nanosponge (NS) was synthesized using diphenyl carbonate (DPC) as a cross-linker to encapsulate the antitumor drug cyclophosphamide (CYC), thus obtaining the NSs-CYC system. The formulation was then associated with magnetite nanoparticles (MNPs) to develop the MNPs-NSs-CYC ternary system. The formulations mentioned above were characterized to confirm the deposition of the MNPs onto the organic matrix and that the superparamagnetic nature of the MNPs was preserved upon association. The association of the MNPs with the NSs-drug complex was confirmed through field emission scanning electron microscopy, energy dispersive spectroscopy, transmission electron microscopy, X-ray photoelectron spectroscopy, dynamic light scattering, ζ-potential, atomic absorption spectroscopy, X-ray powder diffraction, selected area electron diffraction, and vibrating-sample magnetometer. The superparamagnetic properties of the ternary system allowed the release of CYC by utilizing magnetic hyperthermia upon the exposure of an alternating magnetic field (AMF). The drug release experiments were carried out at different frequencies and intensities of the magnetic field, complying with the "Atkinson–Brezovich criterion". The assays in AMF showed the feasibility of release by controlling hyperthermia of the drug, finding that the most efficient conditions were F = 280 kHz, H = 15 mT, and a concentration of MNPs of 5 mg/mL. CYC release was temperature-dependent, facilitated by local heat generation through magnetic hyperthermia. This phenomenon was confirmed by DFT calculations. Furthermore, the ternary systems outperformed the formulations without MNPs regarding the amount of released drug. The MTS (3-(4,5-dimethylthiazol-2-yl)-5-(3-carboxymethoxyphenyl)-2-(4-sulfophenyl)-2*H*-tetrazolium) assays demonstrated that including CYC within the magnetic NS cavities reduced the effects on mitochondrial activity compared to those observed with the free drug. Finally, the magnetic hyperthermia assays showed that the tertiary system allows the generation of apoptosis in HeLa cells, demonstrating that the MNPs embedded maintain their properties to generate hyperthermia. These results suggest that using NSs associated with MNPs could be a potential tool for a controlled drug delivery in tumor therapy since the materials are efficient and potentially nontoxic.

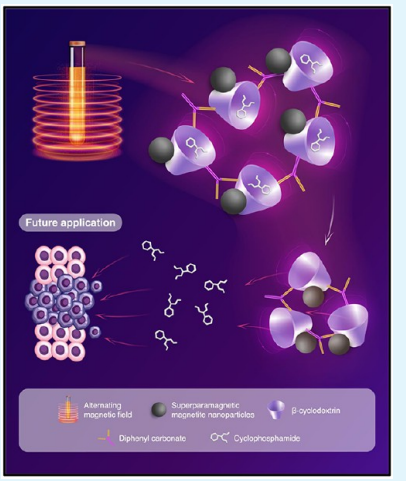

KEYWORDS: *β-cyclodextrin-based polymers, inclusion compounds, superparamagnetic ferrofluid, hyperthermic drug release, drug delivery, tumor therapy*

1. INTRODUCTION

Controlled drug release is one of the most important innovations in cancer treatment today. Anticancer drugs are often restricted due to their poor physicochemical and biopharmaceutical properties, and their low specificity and solubility are challenges that limit their use and effectiveness.[1,2] Cyclophosphamide (CYC) is an anticancer drug used to treat and manage neoplasms, such as multiple myeloma or breast cancer, that exerts its anti-neoplastic effects through the formation of cross-links within DNA, inducing apoptosis. Nevertheless, as alkylating agents can damage both normal and cancer cells, the use of CYC also presents risks of serious side effects, which include hemorrhagic cystitis, alopecia, nausea, sterility, and heart failure.[3]

Special Issue: Forum Focused on South American Authors

Received: December 1, 2023
Revised: April 6, 2024
Accepted: April 11, 2024

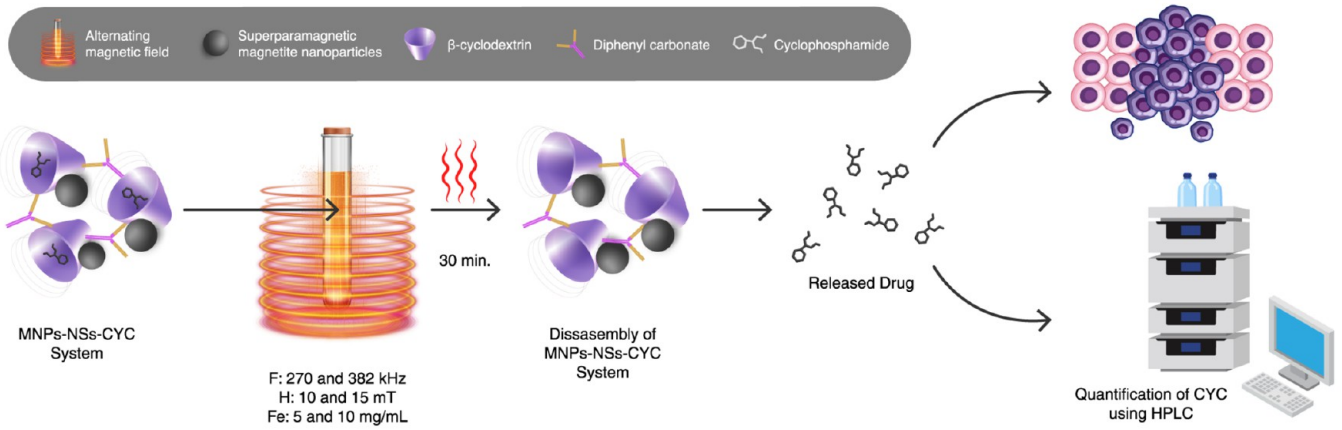

Figure 1. Schematic representation of the drug release process from the MNPs-NSs-CYC system, which is triggered by magnetic hyperthermia.

In recent years, the complexation of some compounds with cyclodextrins (CDs) has emerged as another way of solving the low specificity and solubility problem.[4,5] CD-based nanotechnology proposals are stable, safe, and effective in vivo, with a greater payload for encapsulating hydrophobic drugs for drug delivery.[6,7] In this regard, polymeric cyclodextrins (pCDs), also called nanosponges (NSs), have attracted more attention by combining the advantages of polymer materials (high molecular weight and ability to trap guest molecules in the interspace) with the main advantage of a CD (capture guest molecules and form a clathrate).[8,9] This gives NSs more versatility than natural macrocycles and other chemically modified nonpolymeric derivatives. CD-based NSs have evolved as a promising delivery system to enhance the oral bioavailability and dissolution rate of hydrophobic drugs. NSs are nanosized structures that can be synthesized through the reaction of CDs with a cross-linking agent such as carbonyldiimidazole or diphenyl carbonate (DPC). NSs feature nanosized cavities that allow the solubilization of a plethora of drugs through inclusion and non-inclusion complexation. As such, NSs are increasingly used in biomedicine, the pharmaceutical industry, and drug administration research.[10−12] However, the release of drugs from the cavities of NSs is not site-specific. To overcome such drawbacks, the development of stimulus-responsive NSs has become imperative.

Metallic nanoparticles play an essential role in nanochemistry due to their ability to absorb and scatter electromagnetic radiation.[13−16] Nanoparticles are widely employed in medicine as a promising aspect of ongoing nanotechnology advancements. Active research has focused on the applications of this technology in drug administration, cancer diagnosis, and treatment.[17−20] Metallic nanoparticles can be easily engineered by tuning their size, shape, and surface chemistry. Studies have shown that these characteristics improve the safety and site-specific drug delivery. Moreover, the use of nanoparticles enables controlled drug release, which is critical to achieving efficient therapeutic effects and reducing toxicity and side effects. Stimuli-responsive carriers based on NSs and metallic nanoparticles have been studied as drug delivery systems. A recent study reported the synthesis and characterization of inclusion compounds (ICs) of NSs based on β-CD with the antitumor drugs melphalan (MPH) (also known as alkeran) and CYC conjugated to gold nanoparticles.[21] Drug release promoted by laser irradiation was studied. Furthermore, ICs consisting of NSs and gold nanorods have been synthesized and characterized for potential applications in near-infrared (NIR-II) drug delivery systems using local photothermia.[22]

Extensive research has also been conducted on superparamagnetic nanoparticles due to their potential use in environmental and biomedical applications.[23−26] Hyperthermia therapy has been employed for the treatment of tumors, offering the possibility of targeted nanoscale energy delivery to reach deep tissues using magnetic nanoparticles.[27,28] Superparamagnetic nanoparticles have the potential to be injected directly into cancer tumors or administered intravenously and they can be targeted to tumors by utilizing a combination of the enhanced permeation and retention effect and active targeting through surface ligands.[29−31]

This targeting can lead to the localization of nanoparticles in the extracellular matrix surrounding cancer cells or their uptake and accumulation in intracellular structures such as vesicles, endosomes, and lysosomes.[32,33]

Studies have reported that low-frequency (less than 300 Hz) static magnetic fields exert antitumor effects that are independent of thermal effects. Magnetic fields inhibit cell growth and proliferation, induce cell cycle arrest and apoptosis, regulate the immune system, and inhibit angiogenesis and metastasis.[34−37] Magnetic fields facilitate the action of chemotherapeutic drugs by forming tiny pores on the cell membrane surface, and they enhance the inhibitory effect by regulating apoptosis and the proteins associated with the cell cycle. Currently, magnetic fields are employed in research to deliver drugs to tumors that are led by magnetic nanoparticles. In addition, the application of a high-frequency alternating magnetic field (AMF) induces the release of energy in the form of heat, a mechanism called magnetic hyperthermia. This effect provides a promising strategy for cancer treatment by increasing the cellular temperature within the range of 41−45 °C.[38−40] Numerous studies have been carried out to explore alternative methods for regulating heat production. For example, ferrofluid hyperthermia is a procedure that entails injecting ferrofluid into tissue and exposing it to AMF, resulting in an increase in the temperature in the area. Due to the oscillation of the magnetic moment of metal oxide nanoparticles, heat is released to neighboring tissues.[41−43]

Despite significant advancements in drug delivery systems, there is a notable gap in the literature regarding the release of anticancer compounds from supramolecular NSs triggered by magnetic hyperthermia. In this context, this study explored a ternary system (see Figure 1) comprising a β-CD-based

https://doi.org/10.1021/acsami.3c18038
ACS Appl. Mater. Interfaces XXXX, XXX, XXX−XXX

nanosponge (NS), the anticancer drug CYC, and superparamagnetic magnetite nanoparticles (MNPs). This approach involved encapsulating CYC within a NS matrix to develop the NSs-CYC inclusion compound. MNPs were associated with the NSs-CYC complex to form a superparamagnetic ternary system. The superparamagnetic nanoparticles embedded in the NSs-CYC complex were able to disrupt the ternary system and release the loaded drug upon exposure to an AMF. The feasibility of CYC release was assessed as a function of Fe content, frequency, magnetic field intensity, and temperature increase. Additionally, we evaluated the biocompatibility of the NSs-CYC and MNPs-NSs-CYC complexes in comparison with the free drug. Furthermore, our research evaluated the effects of magnetic hyperthermia and CYC through experiments conducted with HeLa cell lines, aiming to provide valuable insight into localized drug delivery systems. To the best of our knowledge, there have been no reports on the release of anticancer compounds from NSs supramolecular systems by magnetic hyperthermia. Thus, this discovery holds promise as a potential technology for localized drug delivery systems.

2. EXPERIMENTS AND METHODS

2.1. Materials/Chemicals and Reagents. Anhydrous β-cyclodextrin, $C_{42}H_{70}O_{35}$, 97%, 1134.98 g/mol; cyclophosphamide, $C_7H_{15}Cl_2N_2O_2P$, 90%, 261.1 g/mol; diphenyl carbonate, $C_{13}H_{10}O_3$, 99%, 214.2 g/mol; iron(III) chloride, $FeCl_3$, 97%, 162.2 g/mol; iron(II) chloride tetrahydrate, $FeCl_2{\cdot}4H_2O$, 97%, 198.8 g/mol; sodium hydroxide, NaOH, 98%, 40.0 g/mol; polyethylenimine (PEI), H-$(NHCH_2CH_2)_nNH_2$, ≥99.9%, average M_w 25000 Da; and nanopure water were purchased from Merck (Merck, Darmstadt, Germany) and used as received. Aqua regia (3 HCl:1 HNO_3) and Milli-Q water were used to wash all glassware to synthesize the NSs, MNPs, and the ternary system. Cell culture-treated plates and flasks were purchased from Falcon. Tetrazolium inner salt (MTS) and phenazine methosulfate (PMS) were purchased from Promega.

2.2. Preparation of MNPs and NSs. Magnetite nanoparticles were synthesized using the coprecipitation method as previously reported.[44] Briefly, 4 mL of 0.1 M $FeCl_3$ and 1 mL of 0.1 M $FeCl_2$ were mixed and heated to 90 °C in a round-bottom flask under an Ar atmosphere to prevent oxidation of the precursors. In addition, a dropwise addition of a previously prepared solution of 1 M NaOH (50 mL) was performed. Subsequently, 2.1 g of PEI (25000 Da) was dissolved in water and added to the solution. The mixture was stirred for 30 min until a black ferrofluid was formed, and then cooled to room temperature. The precipitate was separated using a neodymium magnet of 5000 G, washed several times with deionized water, oven-dried at 80 °C for 24 h, and stored at 4 °C to prevent its oxidation to maghemite.

β-Cyclodextrin-based NSs were synthesized using a previously reported melting method.[45] Three β-CD NSs were prepared using different β-CD/DPC molar ratios (1:2, 1:4, and 1:8). DPC was melted and further mixed with β-CD, following magnetic stirring at 90 °C for 5 h. The obtained NSs were washed thoroughly with deionized water and ethanol to remove the unreacted precursors. Finally, the polymers were extracted in a Soxhlet apparatus with acetone to remove phenol byproducts and dried in an oven at 80 °C for 24 h.

2.3. Preparation of the NSs-CYC Formulation. CYC was loaded in the cavities of the synthesized NSs following reported methods.[46,47] Concentrated solutions of the drug (0.03 mg/mL) were prepared in a hydroethanolic solution (20% (v/v)), stirred for 24 h and filtered using a 0.45 μm membrane. In addition, 50 mg of NSs was added to a 10 mL solution of CYC and stirred for another 24 h. Finally, the complexes were centrifuged (20 min at 3000g), and the supernatant was recovered and freeze-dried for 72 h.

2.4. Deposition of MNPs onto the NSs-Drug Systems. The MNPs-NSs-drug ternary systems were prepared by mixing MNPs with the obtained NSs-drug formulations, as previously described.[26] A 20 mg amount of NSs-CYC was stirred in 50 mL of an MNPs dispersion. After 30 min, the NSs-drug complexes underwent a transformation in color, transitioning from a white hue to a black-brownish shade. The ternary systems were recovered by centrifugation (20 min, 3000 g) and then freeze-dried. The magnetic response of the developed MNPs-NSs-CYC complex was evaluated by using a 5000 G neodymium magnet.

2.5. Characterization Methods. The incorporation of CYC into the cavities of NSs was examined by using proton nuclear magnetic resonance (^{1}H NMR) analysis, which was conducted on a Bruker Advance 400 MHz spectrometer at 300 K. Stock solutions of the samples were prepared using deuterated dimethyl sulfoxide (DMSO-d_6) as the solvent. The data underwent processing using tetramethylsilane (TMS) as an internal reference.

The morphologies of the resulting NSs-CYC and MNPs-NSs-CYC complexes were examined by using field emission scanning electron microscopy (FE-SEM) with an INSPECT-F50 FEI instrument operating at an acceleration voltage of 20 kV. The deposition of MNPs onto the organic matrix was assessed through the utilization of energy dispersive spectroscopy (EDS) and elemental mapping techniques, together with the determination of the elemental composition of the samples. The average particle size of the deposited MNPs was determined by using transmission electron microscopy (TEM) with a Hitachi model HT-7700 microscope operating at 120 kV. Selected area electron diffraction (SAED) was utilized to obtain diffraction patterns and determine the crystalline structure of the embedded MNPs.

The crystalline structures of CYC, NSs, NSs-CYC, and MNPs-NSs-CYC were analyzed by using powder X-ray diffraction (XRPD) with a Bruker D5000 diffractometer. The source of radiation was Cu Kα_1. The experiment utilized a Ni filter and gathered data within an angular range of 20−70° 2θ and scan speed of 0.05°/s.

The hydrodynamic diameters (D_h), polydispersity indexes (PDIs), and ζ-potentials of NSs, the NSs-CYC complex, MNPs, and the MNPs-NSs-CYC ternary system were determined using a dynamic light scattering (DLS) Zetasizer NanoS series, Malvern, operating at 298 K. Prior to measurements, all of the samples were diluted in a low-ionic-strength buffer solution (KH_2PO_4, 1 mM, pH 7).

The interactions between the NSs-drug complex and MNPs were assessed using X-ray photoelectron spectroscopy (XPS). The XPS spectra were acquired by using a PerkinElmer 1257 photoelectron spectrometer. The energy calibration was conducted by assigning a binding energy of 284.8 eV to the C−C component.

Fourier transform infrared (FT-IR) spectra of CYC, NSs, and NSs-CYC were obtained using a Jasco 4600 spectrometer 4600 equipped with a ZnSe crystal and a deuterated L-alanine-doped triglycine sulfate detector. The analysis was performed by acquiring 150 scans per sample within a wavelength range of 400−4000 cm^{-1} at a temperature of 298 K. Corrections for KBr, CO_2, and H_2O were applied using the Spectra Manager Software.

The Raman spectra of CYC, NSs, and NSs-CYC were analyzed using a WI Tec SNOM/Raman microscope Alpha 300 with a 785 nm laser and 50× objective. The Raman spectra were obtained under the following conditions: a range of 200−1700 cm^{-1}, ten acquisitions, 10 s of integration time per spectrum, and quenching of intrinsic fluorescence using gold coating prepared by sputtering.

The saturation magnetization of MNPs and the ternary system were determined using a custom-made vibrating sample magnetometer (VSM) (CEDENNA, Universidad de Santiago de Chile). The hysteresis loops were obtained at 300 K, while the magnetic field was cycled between −4 and 4 T.

The Fe concentrations in MNPs and the MNPs-NSs-CYC systems were determined by using atomic absorption spectroscopy (AAS) with a PerkinElmer 5100 atomic absorption spectrophotometer. Prior to the analysis, the samples were digested with 1 mL of 0.25 M HNO_3.

2.6. Loading Capacities and Encapsulation Efficiencies. The loading capacities (LC%) and encapsulation efficiencies (EE%) of the developed formulations were calculated using eq 1 and eq 2, respectively:[48,49]

$$\mathrm{LC\%} = \frac{\text{mass of loaded drug (mg)}}{\text{mass of NSs (mg)}} \times 100 \quad (1)$$

https://doi.org/10.1021/acsami.3c18038
ACS Appl. Mater. Interfaces XXXX, XXX, XXX−XXX

$$\text{EE\%} = \frac{\text{concentration of loaded drug (mM)}}{\text{concentration of initial drug (mM)}} \times 100 \quad (2)$$

2.7. Drug Release Assays through Magnetic Hyperthermia. The effect of the AMF on drug release was elucidated using Magnetherm DS2 equipment (Nanotherics, Warrington, U.K.). This device can operate at varying frequencies (270 and 381 kHz) and magnetic fields (10 and 15 mT) in order to analyze the temperature increase when the samples are exposed to the AMF. The magnetic field was applied using the drug release option of the Magnetherm equipment connected to a power supply. The samples were prepared in phosphate buffered saline (PBS, pH 5.8) to mimic a tumor environment. A 5 mg amount of each sample was put on a dialysis tube (Pur-A-Lyzer, 6−8 kDa, Sigma-Aldrich) along with 2 mL of PBS, and the tube was then placed in the drug release compartment. The system was connected to a thermoregulated bath, and the dialysis tube was placed in a container with 50 mL of PBS (release medium). Then, the temperature was recorded by using a fiber optic temperature sensor. After 30 min, the medium containing the released drug was recovered. The concentration of CYC in the receiving phase was measured using high-performance liquid chromatography (HPLC) with the following conditions: a C_{18} column; a water−acetonitrile−methanol (68:19:13 (vol %/vol %)) mobile phase; the λ detector at 254 nm, a flow rate of 0.6 mL/min, total run time of 15 min, and elution time of 3 min. The NSs-CYC formulation was also exposed to AMF as a control to determine the effect of the MNPs on the controlled drug release. The percentages of drug release (DR%) were calculated as follows (eq 3):

$$\text{DR\%} = \frac{\text{amount of released drug (mM)}}{\text{amount of drug in the ternary system (mM)}} \times 100 \quad (3)$$

The heat generated by bare MNPs and MNPs-NSs-CYC exposed to the AMF was quantified using specific absorption rate (SAR)[50] values, calculated using eq 4:

$$\text{SAR} = \frac{\rho C_w}{\text{mass of MNPs}}(\Delta T/\Delta t) \quad (4)$$

where ρ is the density of the colloid (0.995 g/mL), C_w is the specific heat capacity of the medium (4000 kJ kg^{-1} K^{-1}), mass of MNPs is the concentration of MNPs in the suspension (mg/mL), and $\Delta T/\Delta t$ is the heating rate, which was obtained by calculating the slope of a linear fit of temperature increase vs the initial time interval.

2.8. Theoretical Calculations. The initial adsorption configurations of the NSs-CYC complex were found in the Adsorption Locator module of the Materials Studio. This was achieved through a Metropolis Monte Carlo search in a large conformational space, where simulated annealing between 100 and 1.0×10^5 K was employed to locate the global minimum adsorption conformations. Further geometry optimizations of the initial 10 structures with the minimum energy were carried out using the density functional theory (DFT) level in ORCA 5.0, without any geometrical constraints.[51] In order to establish the relative probability of each conformation at room temperature (298.15 K), a Boltzmann distribution function was employed to select the most favorable ground state. The B3LYP functional was used alongside the all-electron def2-SVP basis sets, incorporating the DFT-D3 dispersion correction with the Becke−Johnson damping function for both the SCF energies and gradients. The universal solvation model (SMD), which uses the charge density of a solute molecule interacting with a continuum description of the solvent, was used to incorporate the continuum effects of the solvent in water.

The interaction energies were computed as (ΔE_{int}):

$$\Delta E_{int} = E_{CD-CYC} - (E_{CD} + E_{CYC}) \quad (5)$$

where $E_{CD\text{-}CYC}$, E_{CD}, and E_{CYC}, and are the total energies of the free β-CD, free CYC, and the β-CD-CYC complex, respectively. Therefore, the greater the negative ΔE_{int} values, the higher the stability of the complex. The geometrical counterpoise method was utilized to rectify basis set superposition errors. The Q-Chem 6.1 software was utilized to perform energy decomposition analysis based on precisely localized molecular orbitals [ALMO-EDA]. This approach allowed for the separation of interaction energies in the continuum solvent into distinct physical contributions.[52] Thus, ΔE_{int} can be split into six different terms:

$$\Delta E_{int} = \Delta E_{ELEC} + \Delta E_{DISP} + \Delta E_{POL} + \Delta E_{CT} + \Delta E_{PAULI} + \Delta E_{PREP} \quad (6)$$

where ΔE_{ELEC}, ΔE_{DISP}, ΔE_{POL}, and ΔE_{CT} represent the energy stabilization due to electrostatic interactions (Coulombic attractions), dispersion forces (van der Waals interactions), polarization (induced electrostatic effects), and charge transfer (inter- and intramolecular charge flow between fragments), respectively. When two fragments are in close proximity, the Pauli repulsion phenomenon leads to energy destabilization (ΔE_{PAULI}), and the energy required by the isolated fragments to adopt the complex geometry is known as ΔE_{PREP}. Additionally, the Independent Gradient Model (IGM) with the Hirschfeld partition was used to define the signature of intermolecular interactions; this index introduces the δg^{inter} descriptor that uniquely defines intermolecular interaction regions: $\delta g^{inter} = |\nabla\rho^{IGM,inter}| - |\nabla\rho|$, where $\nabla\rho$ stands for the electron density gradient, and $\nabla\rho^{IGM,inter}$ corresponds to an upper limit for $\nabla\rho$. Wave function analyses were performed using the Multiwfn 3.8 program.

2.9. Mitochondrial Activity Assays. Mitochondrial activity assays were performed by MTS using a Cell Titer 96 Aqueous Solution Cell Proliferation Assay (Promega). The experiments were conducted in accordance with the manufacturer's recommendations. Briefly, 5000 cells were seeded in each well of 96-well plates with 100 μL of Dulbecco's modified Eagle medium (DMEM) heated to a temperature of 335 K and subsequently removed after 24 h. The cells were incubated for an additional 24 h with 1 to 1 serial dilution of NSs, CYC, NSs-CYC, and MNPs-NSs-CYC. The concentrations of all samples ranged from 0.03, 0.015, 0.008, and 0.003 mg/mL in 1% dimethyl sulfoxide (DMSO), and the concentration of NSs ranged from 20.0, 10.0, 5.0, and 2.5 mg/mL. The volume was then completed with DMEM. Afterward, phenol red-free DMEM (Gibco) containing the MTS/PMS reagent was added to replace the medium and incubated for 1 h at 335 K. The absorbance of all of the samples was measured with a microplate reader at 490 nm/655 nm (Synergy Mx, Biotek). The fluorescence for each experiment was corrected by subtracting the mean fluorescence value obtained from a triplicate set of control wells without cells. Mitochondrial activity was calculated with respect to the untreated control media. Each experiment was performed by using three technical replicates and two biological replicates.

2.10. Magnetic Hyperthermia Assay in HeLa Cells. HeLa cell lines (obtained from ATCC) were cultured in a concentration of 500000 cells/mL in a 35 mm Petri dish (Corning) with 1 mL of DMEM culture medium supplemented with 1 mM sodium pyruvate, 100 IU/mL penicillin, 100 μg/mL streptomycin, and 10% fetal bovine serum and kept in a humid environment at 37 °C with 95% air and 5% CO_2. Next day, the Petri dishes were divided into 8 treatment groups ($n = 3$), which were treated overnight: (1) control with AMF; (2) control without AMF; (3) MNPs, 0.5 mg/mL; (4) MNPs, 1 mg/mL; (5) MNPs-NSs-CYC, 2.5 mg/mL; (6) MNPs-NSs-CYC, 5 mg/mL; (7) NSs, 2 mg/mL; and (8) NSs, 4 mg/mL, and treated overnight, After, the Petri dishes were placed in a cell live module from hyperthermia equipment and treated for 30 min with $F = 734$ kHz and $H = 10$ mT. Then, the cells were placed in the incubator and evaluated after 72 h of treatment to determine the number of cells. Finally, the cells were stained with a Hoechst solution (Invitrogen) for 15 min and evaluated by fluorescence microscopy to determine the number of cells per field of view.

2.11. Statistical Analysis. All the experiments were carried out in triplicate, and the results were represented as mean ± SD. A one-way ANOVA statistical analysis followed by a Dunnett test was conducted using GraphPad Prism 9.0.0 (San Diego, CA, USA) to assess the statistical significance of the measurements (***$p < 0.001$ or *$p < 0.01$).

https://doi.org/10.1021/acsami.3c18038
ACS Appl. Mater. Interfaces XXXX, XXX, XXX−XXX

3. RESULTS AND DISCUSSION

3.1. Encapsulation Efficiency (EC%) and Loading Capacity (LC%) of NSs Using Different Cross-Linking Degrees and β-CD/DPC Molar Ratios. All prepared NSs (1:2, 1:4, and 1:8) were loaded with free CYC. The EC% and LC % of NSs were further evaluated (see Table 1). Compared to the other NSs produced, the NSs carrier in the 1:4 molar ratio of NSs-CYC formulations exhibited higher EC% and LC% values. These results suggest that the degree of cross-linking affects the efficiency of complexation and the availability of supramolecular sites in the NSs. For instance, a molar ratio of 1:2 would be insufficient to develop enough cross-linking and interstices for drug inclusion. In turn, a greater molar ratio would result in increased cross-linking and, thus, hinder the inclusion of CYC into the NS cavities.[53−55] These results led to the conclusion that a molar ratio of 1:4 would be optimal for cross-linking the drug CYC. Therefore, the NSs-CYC (1:4) formulation was selected for association with MNPs, local hyperthermia, and drug release assays.

Table 1. Encapsulation Efficiencies (EC%) and Loading Capacities (LC%) of NSs with Different β-CD/DPC Molar Ratios

System	EC%	LC%)
NSs-CYC (1:2)	88.3 ± 3.7	21.1 ± 3.8
NSs-CYC (1:4)	95.3 ± 1.8	29.9 ± 4.1
NSs-CYC (1:8)	79.9 ± 3.3	18.8 ± 5.7

3.2. Characterization of NSs-CYC Inclusion Compound. The NSs-CYC formulation was characterized by using ^{1}H NMR, FE-SEM, EDS, XRPD, FT-IR, and Raman spectroscopy. ^{1}H NMR spectra of CYC, NSs, and the NSs-CYC complex are shown in Figure 2.

The inclusion of CYC within the supramolecular sites of NSs can be confirmed by analyzing the changes in the chemical shifts of all protons. The proton signals of CYC (H′1: δ 3.41; J 6.38; 4H; triplet. H′2: δ 3.83; J 6.38; 4H; triplet. H′3: δ 4.19; J 14.9, 3.0, 2.7; 2H; doublet. H′4: δ 1.83; J 1.40, 10.3, 3.3, 3.0; 1H; doublet. H′5: δ 3.11; J 15.0, 3.3, 2.5; 2H; doublet) evidenced high-field chemical shifts ascribed to changes in the chemical environment of the drug. This can be attributed to the entrapment of CYC within the cavities of NSs, resulting in screening effects and spatial restrictions that contribute to the aforementioned observations. As for the protons of the NSs matrix, the pronounced chemical shifts observed for the H3, H5, and H6 signals, corresponding to the hydrophobic cavities of NSs, strongly suggested the complexation of CYC. In addition, the H1, H4, and H2 signals, which are assigned to the external cavities of NSs, also displayed chemical shifts, evidencing the inclusion of CYC in all of the supramolecular sites formed during the β-CD polymerization process. As shown in Table 2, the chemical shifts of CYC are more pronounced in the protons corresponding to its oxazaphosphinan structure, demonstrating the preferential inclusion of CYC within the hydrophobic sites of NSs.

The formation of the NSs-CYC complex can also be ascertained through FE-SEM and EDS analyses. FE-SEM micrographs of CYC, NSs, and NSs-CYC are shown in Figure 3A−C, respectively.

The acquired images for NSs confirmed its rough surface, whereas CYC displayed a crystalline morphology. The NSs-CYC complex maintained the morphological profile of NSs and the free drug was not observed in the matrix, suggesting the formation of an inclusion compound rather than a physical mixture of NSs-CYC. The elemental composition of NSs-CYC was obtained from EDS analysis, as shown in Figure 3d.

Both NSs and CYC were identified based on the detection of C and O, which correspond to their respective chemical structures. Moreover, the presence of N, Cl, and P was also detected, which can be attributed to the amine, chloroethyl, and oxazaphosporine groups which are inherent to the structure of CYC, further supporting the presence of the NSs-CYC formulation.

XRPD diffractograms of CYC, NSs, and NSs-CYC were performed to elucidate the crystalline or amorphous nature of the drug, the polymeric matrix, and the developed formulation, as shown in Figure 4. The diffractogram of free CYC illustrated sharp diffraction peaks[56] at 2θ of 7.0, 13.9, 15,1, 23.7, 25,3, and 28.1°, evidencing its strong crystalline behavior. The NSs diffractogram displayed fewer peaks, indicating an amorphous form. In the case of the NSs-CYC formulation, the characteristic sharp peaks of CYC were noticeably masked or diminished by the NSs matrix, confirming amorphization of the drug. Crystallinity hinders the solubility of a substance, while an amorphous formulation enhances solubility and dissolution

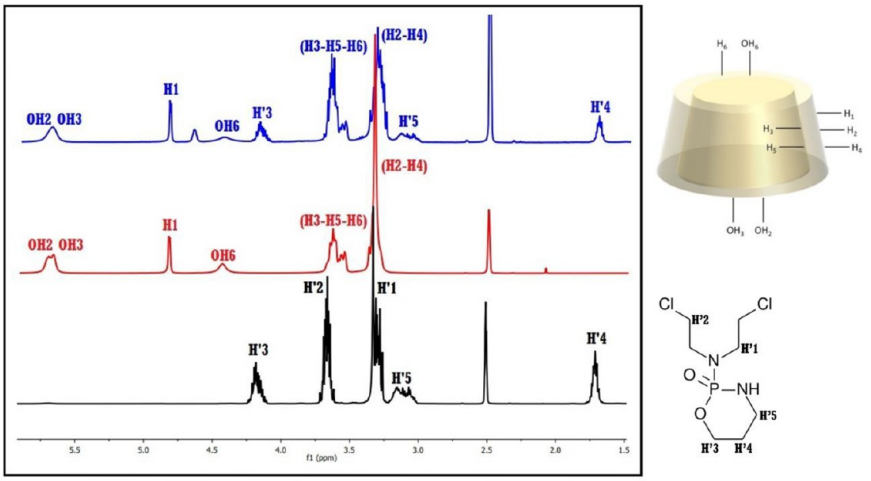

Figure 2. ^{1}H NMR spectra (400 MHz, DMSO-d_6) of CYC (black), NSs (red), and NSs-CYC (blue).

https://doi.org/10.1021/acsami.3c18038
ACS Appl. Mater. Interfaces XXXX, XXX, XXX−XXX

Table 2. Chemical Shifts ($\Delta\delta$) of CYC and NSs before and after the Formation of the NSs-CYC Formulation

System	H1	H2	H3	H4	H5	H6	OH2	OH3	OH6
NSs	4.83	3.30	3.63	3.36	3.58	3.65	5.70	5.68	4.45
NSs-CYC	4.81	3.29	3.58	3.35	3.53	3.62	5.73	5.71	4.43
$\Delta\delta$	0.02	0.01	0.05	0.01	0.05	0.03	−0.03	−0.03	−0.02

System	H′1	H′2	H′3	H′4	H′5
CYC	3.41	3.83	4.19	1.83	3.11
NSs-CYC	3.39	3.81	4.15	1.79	3.06
$\Delta\delta$	0.02	0.02	0.04	0.04	0.05

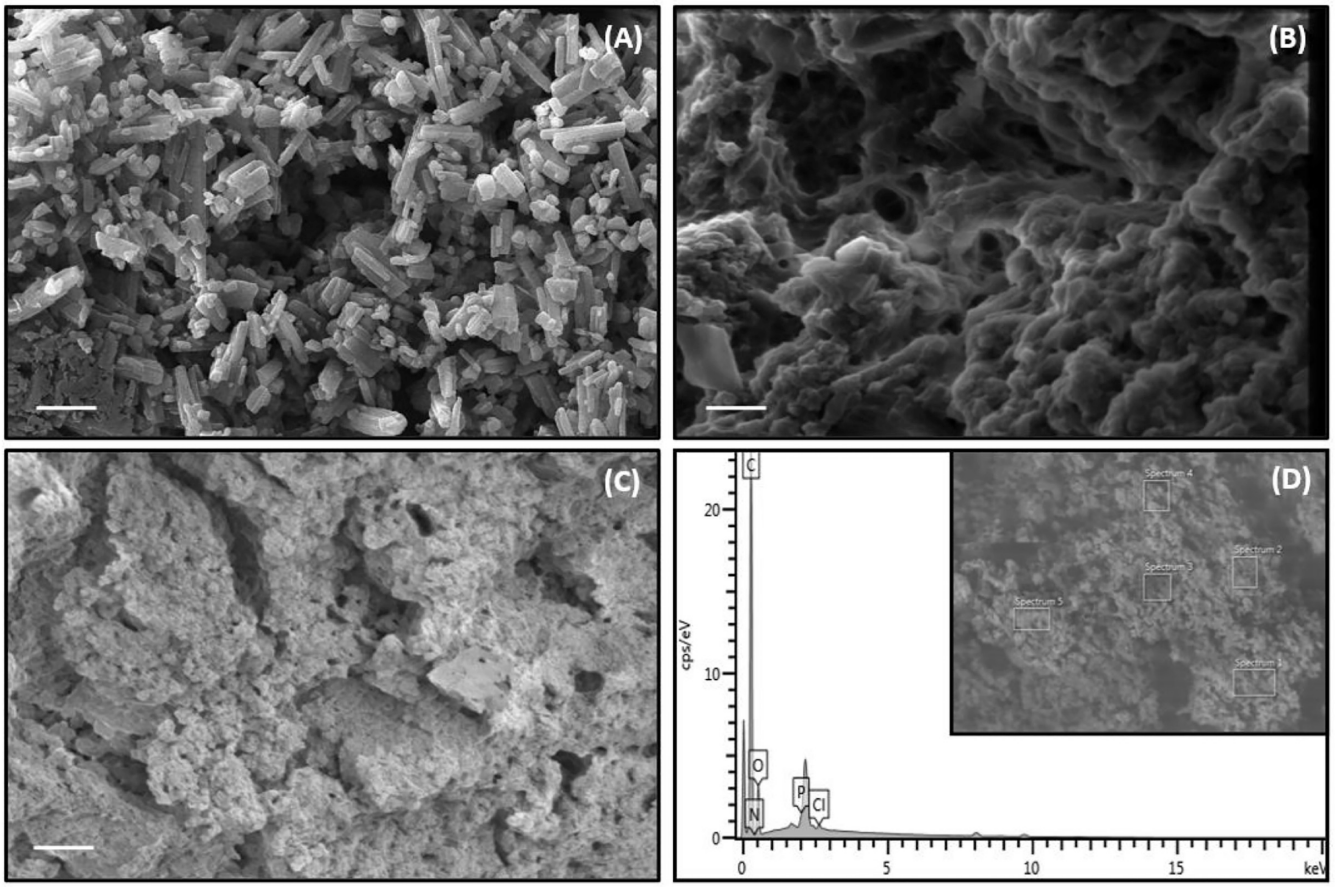

Figure 3. FE-SEM (magnification of 10.00 Kx) of CYC (A), NSs (B), and NSs-CYC (C); EDS of NSs-CYC (D). Scale bar: 10 μm.

rates resulting from higher levels of free Gibbs energy and higher molecular mobility.[57,58]

The CYC, NSs, and NSs-CYC samples were characterized and analyzed by Raman spectroscopy and FT-IR (Figure 5). After obtaining the inclusion complex, Raman and FT-IR spectra can be compared to NSs to observe any differences ascribed to the chemical interaction. In this sense, we expected band shifts and changes in the relative intensities of some signals due to the interaction. The FT-IR spectra of NSs and NSs-CYC revealed the presence of two bands with relative intensities at 1630 and 1750 cm^{-1}. The band found at 1630 cm^{-1} corresponded to water molecules located in the cavities of NSs, while the second signal at 1750 cm^{-1} was ascribed to the overlapping of the stretching modes of C═O and P═O. The increase in the relative absorbance observed in the IR spectra of NSs-CYC can be attributed to this phenomenon. The presence of other weak bands at 1450 and 1340 cm^{-1} were attributed to the vibration of the CYC compound and also supported the formation of the NSs-CYC system.

A signal at 620 cm^{-1} was detected in the Raman spectrum of the NSs-CYC system. The significant relative intensity of this band is a result of the high polarizability of the C−Cl bond, which is influenced by the interaction between CYC and the NSs. This was further corroborated by the absence of this band in the CYC Raman spectrum at 741 cm^{-1}, which was ascribed to the C−Cl deformation.

3.3. Characterization of the MNPs-NSs-Drug Ternary Systems. The association of the MNPs with the NSs (1:4)-CYC complex was confirmed by using FE-SEM, EDS, VSM, TEM, SAED, DLS, ζ-potential, XPS, and AAS analyses.

The TEM analyses of the ternary system (Figure 6A) showed that the MNPs exhibited a spherical morphology, with an average size of 15 ± 0.8 nm (Figure 6B, N = 100). However, the agglomeration of the MNPs was detected, probably due to weak interactions, such as van der Wall forces or magnetic dipoles.[59,60]

https://doi.org/10.1021/acsami.3c18038
ACS Appl. Mater. Interfaces XXXX, XXX, XXX−XXX

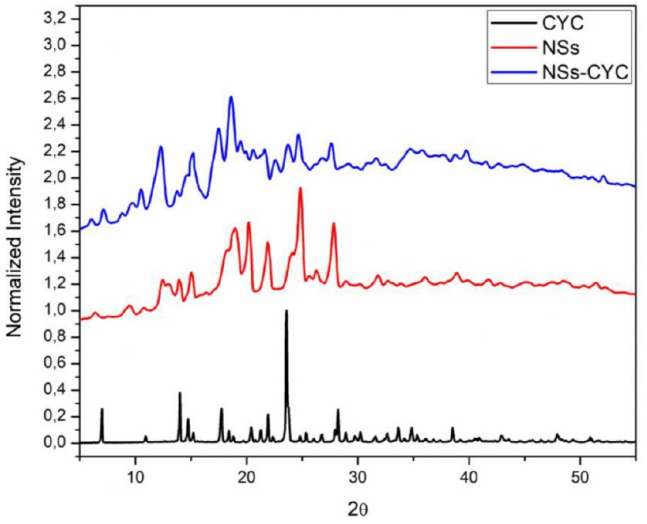

Figure 4. XRPD patterns of CYC, NSs, and NSs-CYC.

The saturation magnetization values (M) were 75.1 and 57.7 emu/g for bare MNPs and MNPs-NSs-CYC, respectively, at 298 K (Figure 7A). Hysteresis was absent, and the coercivity and remanence values were close to zero, thus confirming the superparamagnetic nature of the MNPs upon association.[61,62] The decrease in saturation magnetization values can be attributed to the diamagnetic contribution of the NSs-CYC formulation, which hinders the effective magnetic moment of the ternary system. Furthermore, the interaction between MNPs and the NSs-CYC complex could affect the alignment of the magnetic moments. The Fe 2p XPS spectra of the ternary systems (Figure 7B) depicted a shoulder at 711.1 and 725.1 eV for the Fe $2p_{3/2}$ and Fe $2p_{1/2}$ peaks, respectively. The peak at 711.1 eV was assigned to the Fe(III) occupying the octahedral sites of MNPs[63] intensity can be attributed to the partial oxidation of Fe(II) to Fe(III) at the surface of the NPs or the presence of Fe(III) oxyhydroxides in the outermost layer of the MNPs.[63,64]

The deposition of the MNPs in the NSs-CYC complex was assessed through XRPD (Figure 8A). The diffraction peaks at 2θ of 30.3° (220), 35.5° (311), 43.1° (400), 53.8° (422), 57.3° (511), and 62.7° (440) were consistent with the patterns observed in the inverse spinel structure of magnetite.[63,65,66] The crystalline structure of the MNPs in the ternary systems was also examined and confirmed using SAED analysis (Figure 8B), as the diffraction rings correspond to the lattice planes in the MNPs structure.[67,68]

Finally, the FE-SEM micrographs of the ternary systems (Figure 9A,B) clearly showed that the MNPs were deposited uniformly on the organic substrates, confirming their spherical shape and average size of 15 nm. The EDS mapping (Figure 9C,D) of Fe confirmed the association of MNPs and their homogeneous distribution on the NSs-CYC complexes.

To ascertain colloidal stability, hydrodynamic diameters, monodispersity, and Fe content, various analyses were conducted, including DLS, ζ-potential, polydispersity indexes, and AAS. The results of these analyses were then compared to those of their separate components, as shown in Table 3.

The hydrodynamic diameter (D_h) values ranged from 27 to 259 nm, confirming the nanometric dimensions of the formulated systems. The D_h of bare MNPs was 27 nm, which differed from the data obtained using TEM, since the latter does not consider the hydration layer surrounding the nanoparticle. The observed positive ζ-potential values of MNPs were attributed to their stabilization with PEI, which further decreased when the MNPs were associated with the NSs-CYC system with negative surface charge. The polydispersity index (PDI) of the developed nanosystems indicated their homogeneous nature, since all observed values were below 0.7.[69]

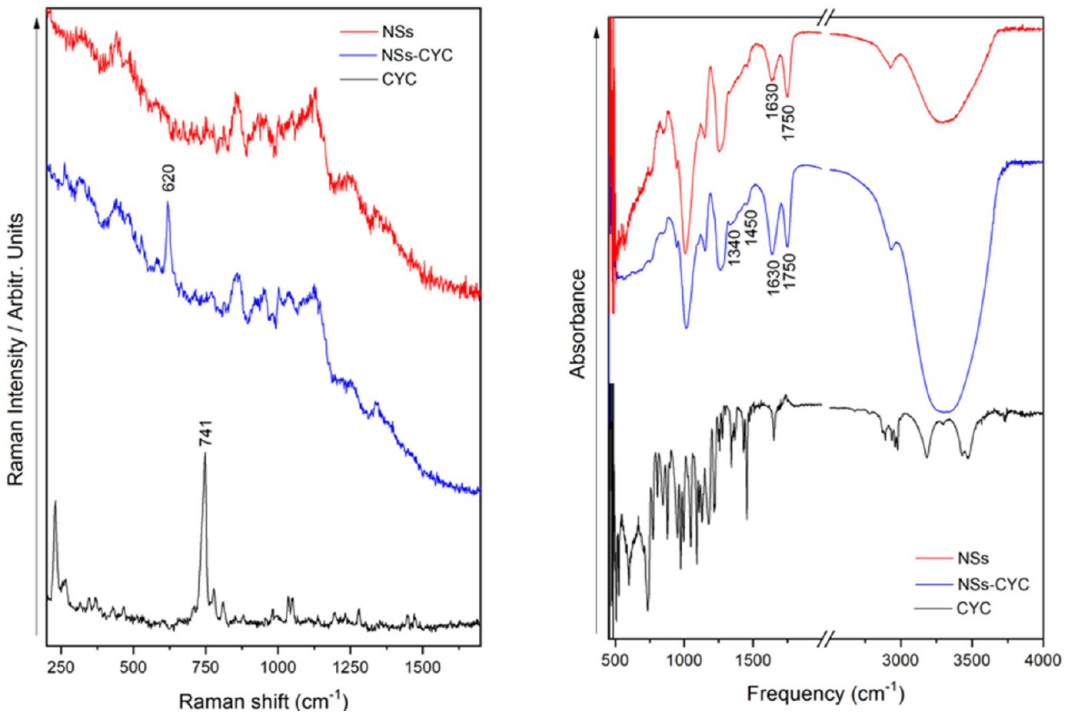

Figure 5. Raman (left) and FT-IR (right) analyses of CYC, NSs, and NSs-CYC.

https://doi.org/10.1021/acsami.3c18038
ACS Appl. Mater. Interfaces XXXX, XXX, XXX−XXX

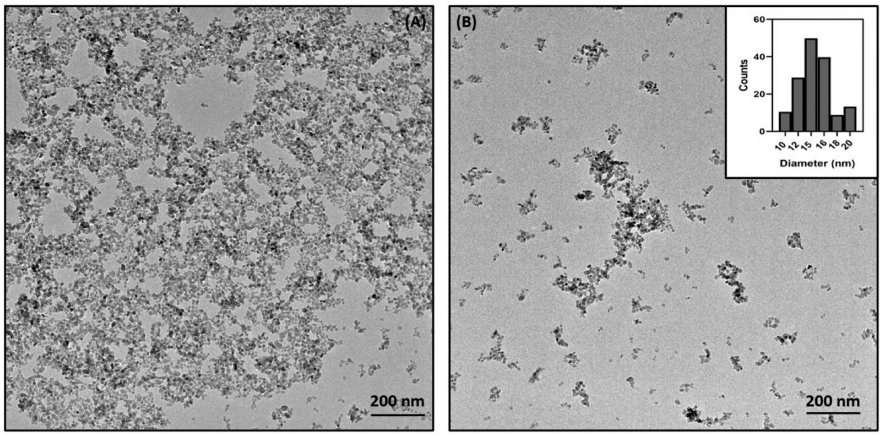

Figure 6. TEM micrograph (A) and size distribution (B) of MNPs deposited on the NSs-CYC formulation. Magnification of 36.00 Kx.

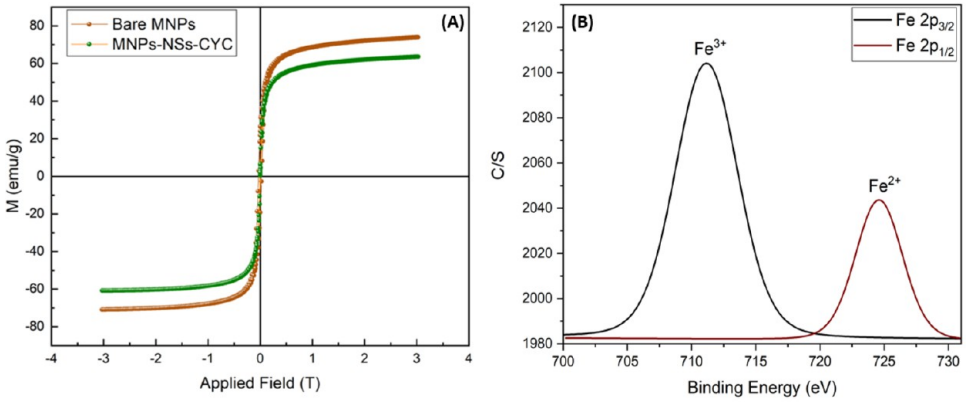

Figure 7. VSM (A) and XPS (B) images of MNPs deposited on the NSs-CYC formulation.

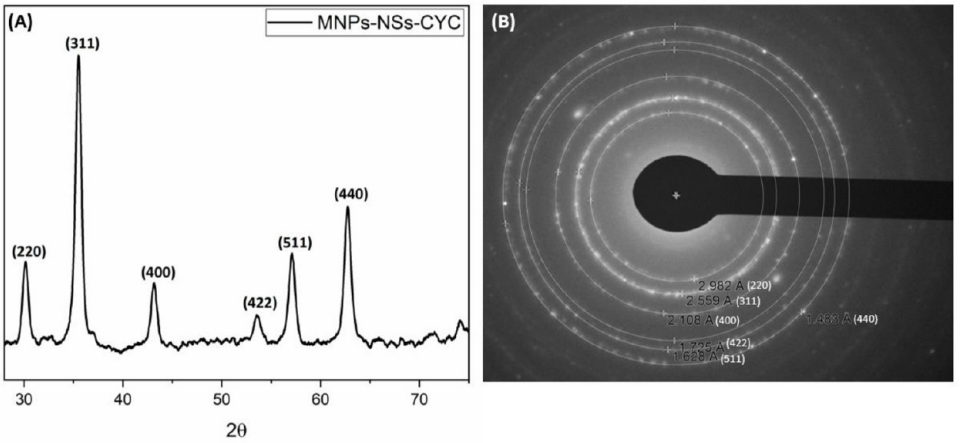

Figure 8. XRPD (A) and SAED patterns (B) of MNPs deposited on the NSs-CYC formulation.

Furthermore, the ζ-potentials ranging from ± 20 to 30 suggested the colloidal stability of all of the samples.[47] AAS was performed to quantitatively analyze the elemental composition of MNPs and the ternary systems, revealing that the Fe content was 251 and 178 mg/mL for bare MNPs and MNPs-NSs-CYC, respectively. These results indicated that the NSs-CYC systems are appropriate substrates for the immobilization of MNPs.

3.4. Local Temperature Increments through Magnetic Hyperthermia and Exposition to an AMF. The influence of an AMF on the MNPs and MNPs-NSs-CYC systems was studied as a function of Fe content (5 and 10 mg/mL), frequencies (270 and 382 kHz), magnetic field intensity (10 and 15 mT), and temperature increase. The temperature increase was measured after 30 min of exposure to the AMF, as observed in Figure 10. We determined the optimal field and frequency values to generate hyperthermia. First, we exposed 5 and 10 mg of MNPs, resuspended in water, to low frequency and high field conditions (F = 270 kHz; H = 15 mT), as well as high frequency and low field conditions (F = 382 kHz; H = 10 mT). An augmented increase in temperature was observed at lower frequencies and higher amplitudes (Figure 10A,B). Therefore,

https://doi.org/10.1021/acsami.3c18038
ACS Appl. Mater. Interfaces XXXX, XXX, XXX−XXX

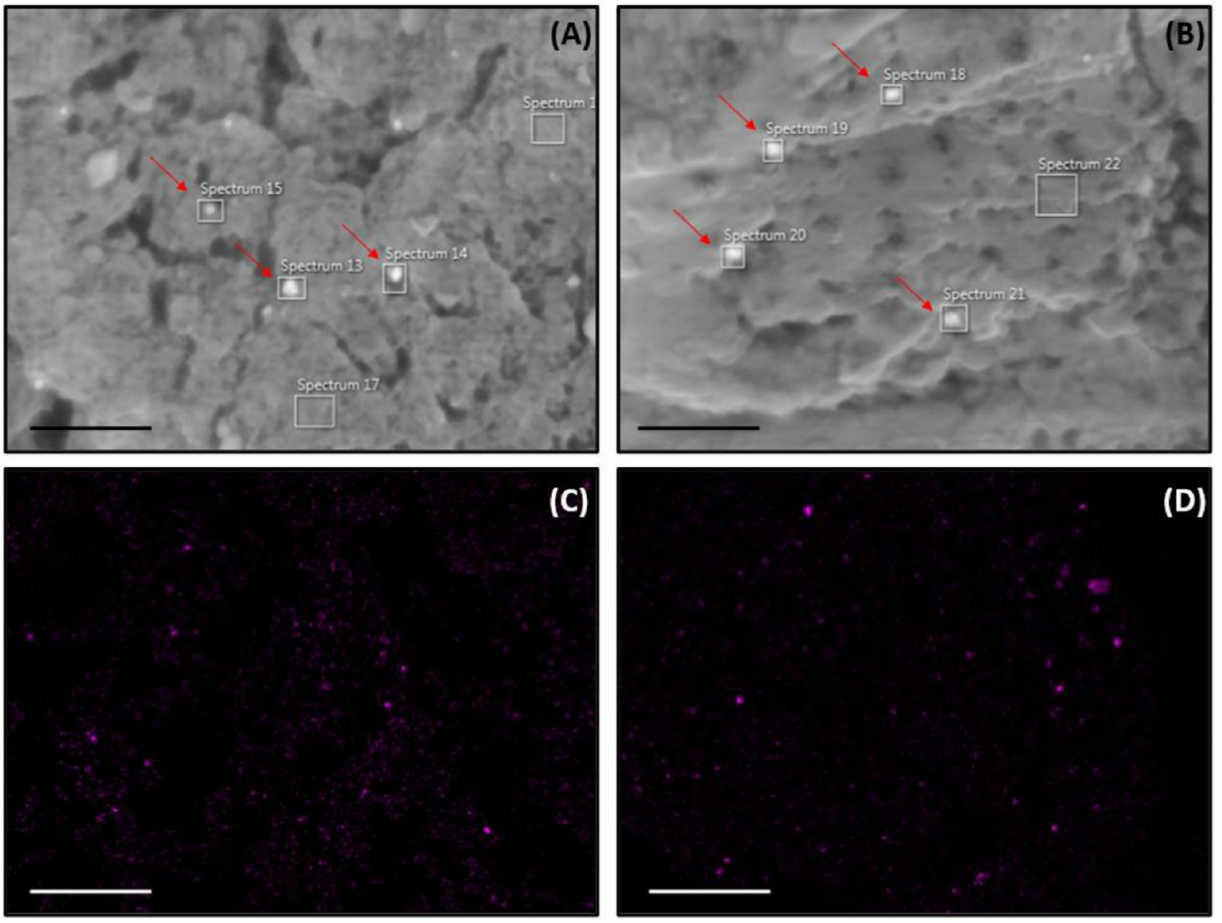

Figure 9. FE-SEM (A, B) and EDS (C, D) of MNPs-NSs-CYC. The red arrows in panels A and B highlight the location of the MNPs embedded in the NSs-CYC formulation. Scale bar = 5 μm.

Table 3. Hydrodynamic Diameter (D_h), ζ-Potential, Polydispersity Index (PDI), and AAS of NSs, NSs-CYT, MNPs, and the MNPs-NSs-CYT System

System	D_h (nm)	ζ-potential (mV)	PDI	Fe content (mg/mL)
NSs	157 ± 21	−31 ± 8	0.28 ± 0.01	
NSs-CYC	243 ± 29	−25 ± 3	0.37 ± 0.05	
MNPs	27 ± 8	+43 ± 9	0.33 ± 0.03	251.3 ± 11
MNPs-NSs-CYC	259 ± 33	+37 ± 5	0.43 ± 0.05	178.1 ± 17

we selected these same parameters for the tests involving the MNPs-NSs-CYC system. The heating capacity of the systems was also compared with NSs (at a ratio of 1:4), MNPs, and the medium (PBS in Milli-Q water) as controls in order to determine whether the local hyperthermia effect may be attributable to the presence of superparamagnetic MNPs in the formulations.

The MNPs-NSs-CYC samples with Fe concentrations of 10 mg/mL exhibited comparable heating to the 5 mg/mL sample after 30 min under a magnetic field intensity of 15 mT and frequency of 270 kHz (7.82 ± 0.42 vs 7.20 ± 0.56 °C temperature increase, respectively), as shown in Figure 10C,D. This effect may occur due to the interference of the NS carrier with the heating and heat transmission capacity of the MNPs, which is crucial for allowing temperature increase. Likewise, upon comparison of the temperature increase produced by bare MNPs to MNPs-NSs-CYC samples, a significant decrease in the generated heat was evident for both concentrations. Therefore, while there was an increase of 37.6 ± 4.5 °C with 10 mg/mL MNPs, the 10 mg/mL MNPs-NSs-CYC complex featured a temperature increase of only 7.82 ± 0.42 °C. This effect could be attributed to several factors. A possibility could be the agglomeration of the MNPs deposited in the NSs-CYC formulation. Agglomeration decreases the effective surface area of the MNPs available for interaction with the AMF, thus reducing heating capacity.[70,71] Likewise, the heating efficiency could decrease due to an increase in the hydrodynamic size, and this effect is attributed to the increase in magnetic interparticle dipolar interaction, which reduces the Neel−Brownian relaxation. Moreover, the diamagnetic nature of NSs does not contribute to Neel mechanisms. Furthermore, there was no rise in temperature when the control systems (NSs and the PBS medium) were exposed to the AMF because in these cases there are no superparamagnetic nanoparticles present to produce local heating. This result confirms that the localized hyperthermia is solely produced by the contribution of the MNPs to the nanocarriers.

https://doi.org/10.1021/acsami.3c18038
ACS Appl. Mater. Interfaces XXXX, XXX, XXX−XXX

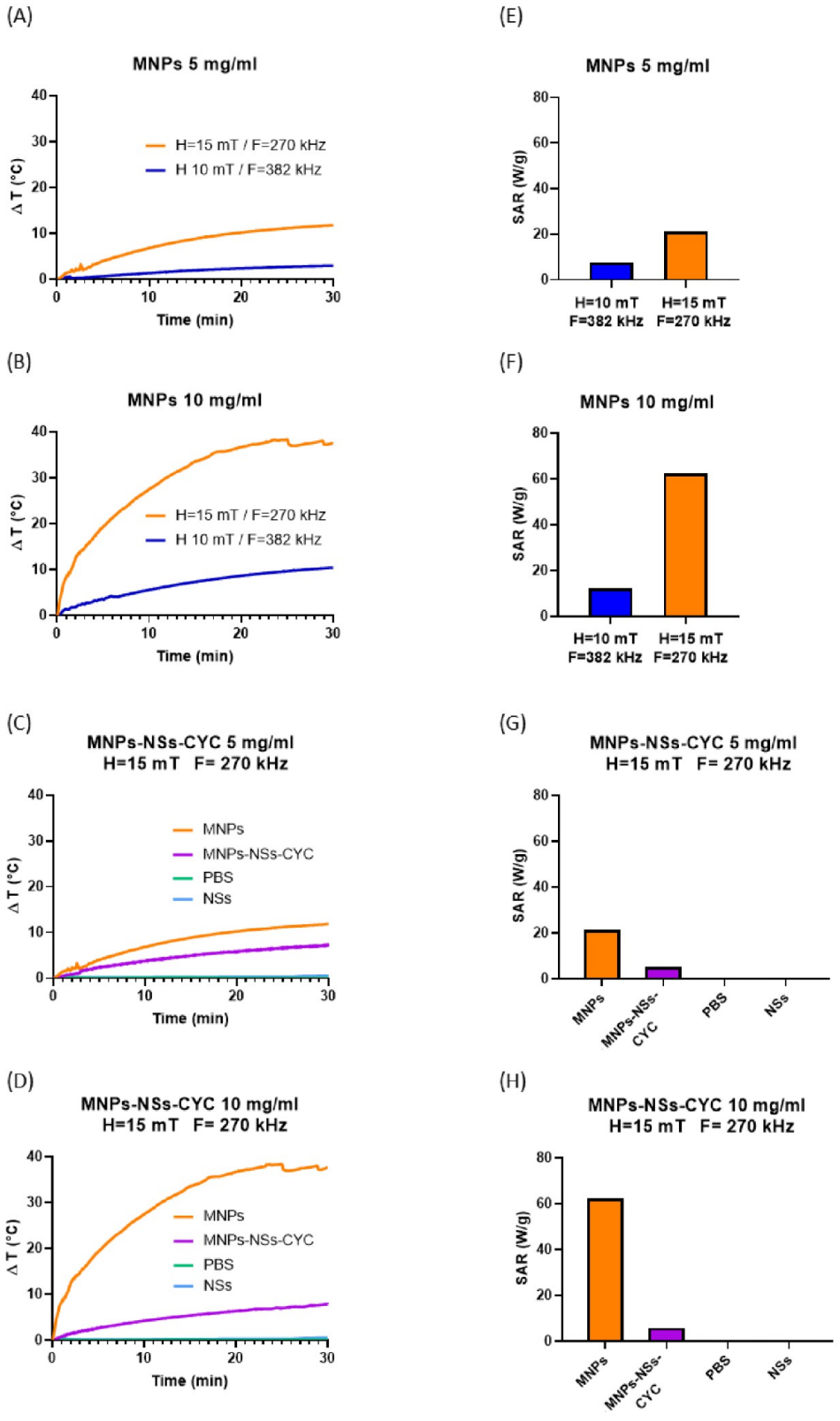

Figure 10. Temperature increment of MNPs (orange and blue), MNPs-NSs-CYC (purple), PBS (green), and NSs (light blue) upon exposure to an AMF, at different Fe contents: MNPs, 5 mg/mL (A); MNPs, 10 mg/mL (B); MNPs-NSs-CYC, 5 mg/mL (C); MNPs-NSs-CYC; 10 mg/mL (D). SAR values (E−H). The data are presented as the mean ± SEM of three independent experiments.

For efficient magnetic hyperthermia treatments, obtaining high SAR values with minimal concentrations of the sample is required. Calculated SAR values for MNPs and MNPs-NSs-CYC are shown in Figure 10E−H. It can be observed that the SAR increases as the concentration of MNPs increases but decreases significantly in the tertiary compound. Many factors

https://doi.org/10.1021/acsami.3c18038
ACS Appl. Mater. Interfaces XXXX, XXX, XXX−XXX

could affect the SAR values such as the size, saturation, hydrodynamic size, and polydispersity of MNPs. As we have already mentioned, the NSs-CYC formulation has a larger hydrodynamic size and can contribute to the agglomeration of MNPs, affecting heat transfer and consequently SAR values. These parameters could be predominant even on the concentration of nanoparticles present, explaining why MNPs-NSs-CYC 5 and 10 mg had similar SAR values (5.3 and 5.8 W g^{-1}).

3.5. Release of CYC from the Cavities of NSs Triggered by Magnetic Hyperthermia. The potential of the developed ternary systems as magnetic nanocarriers for drug delivery was investigated. The conditions used for this experiment were as follows: Fe content of 5 mg/mL, 15 mT, 270 kHz, 30 min, and NSs prepared with a cross-linker ratio of 1:4. The superparamagnetic properties of the MNPs might trigger local hyperthermia in the MNPs-NSs-drug formulation, thus inducing the release of CYC from the cavities of the NSs. The drug release phenomena were also studied in the following control systems: MNPs-NSs-CYC without AMF but exposed to physiological temperature (37−42 °C, C1), NSs-CYC without MNPs and without AMF (C2), NSs-CYC without AMF and MNPs (C3), and NSs-CYC exposed to AMF but without MNPs (C4). These controls were compared with the amount released from the ternary systems to determine whether the guest migrated from the formulations as a result of diffusion or the effects of local hyperthermia. The drug release percentages for each system are shown in Figure 11.

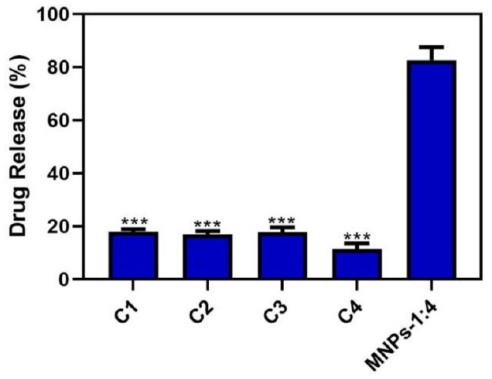

Figure 11. Drug release percentages (%) after 30 min of exposure to the AMF. The data were compared with the systems used as controls and represent the mean ± SEM of three independent experiments. Statistical significance is indicated with ***$p < 0.001$.

The hyperthermia effect produced by the exposure of MNPs to an AMF promoted the disassembly of the ternary system and triggered drug release. The amount of released CYC through passive diffusion (C1−C4) was drastically reduced in all of the control systems, confirming the stability of the systems and that the effect of AMF in the presence of MNPs promoted a faster and more efficient release of the guest. The results indicate that a frequency of 270 kHz, a magnetic field intensity of 15 mT, and an Fe concentration of 5 mg/mL are sufficient for achieving the desired drug release. These parameters fulfill the Atkinson−Brezovich criteria, making them essential factors. For potential biological, clinical, and tumor therapy applications, 50−2000 kHz frequencies are recommended to avoid excessive skeletal muscle stimulation.[72,73] Additionally, the product of magnetic field intensity and frequency should not exceed 4.85×10^9 A m^{-1} s^{-1}.[72−74] The combinations of frequencies and magnetic field intensities used for the drug release experiments fell within the previously proposed values (3.3×10^9 A m^{-1} s^{-1}), suggesting the potential applications of the ternary systems for in vivo studies and physiological conditions.

The CYC release data were fitted to different kinetic models. The Higuchi model was obtained by plotting cumulative drug release (%) vs the square root of time, whereas the Korsmeyer−Peppas model was obtained by plotting the log of cumulative drug release vs the log of time. The Higuchi and Korsmeyer−Peppas models had R^2 values of 0.973 and 0.985, respectively. As a result, the Korsmeyer−Peppas model is better suited for analyzing the drug release profile of the MNPs-NSs-CYC system. The process is affected by conformational changes in NSs caused by swelling or hydrolytic cleavage, which expand the volume of the polymer and enable drug release.[75] CYC is expected to experience noncovalent interactions with the β-CD units or with the differently sized interstices produced during polymerization. The encapsulation of CYC within the polymerization interstices, combined with the complexation capacity of the β-CD monomers, are factors that promote two-step release kinetics.[76]

The morphology and structure of the NSs-CYC-MNPs formulation before and after drug release assays through magnetic hyperthermia was visualized through FE-SEM micrographs. As observed in Figure 12A,B, the exposure to an AMF

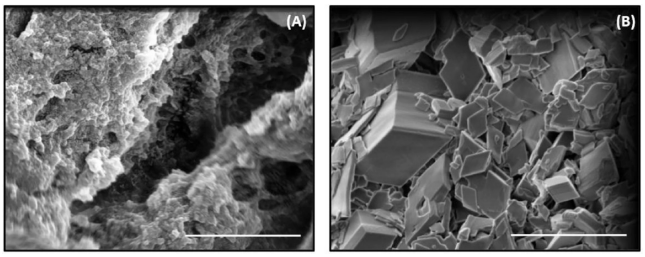

Figure 12. FE-SEM micrographs of the NSs-CYC-MNPs ternary system before (A) and after (B) exposure to the AMF. Scale bar: 2 μm.

might promote the disruption of the systems' integrity, potentially leading to changes in its porous morphology. The localized heating produced by magnetic hyperthermia could have an impact on the structure and conformation of the NSs. This impact is evidenced by degradation of the polymer and changes in the overall structure of the formulation. Furthermore, exposure to an AMF impacts CYC release kinetics and the distribution of the drug within the system, thus contributing to alterations in the observed structure.

3.6. NSs-CYC Interaction Mechanism and Its Role in the Drug Release Process. Density functional theory (DFT) calculations on the NSs-CYC complex revealed that the interaction mechanism was stable and noncovalent. First, the ground state inclusion complex was characterized by the introduction of the *N*-chloroethyl moiety of the drug into the β-CD cavity with intermolecular distances of 1.7 to ~3 Å (Figure 13A). The adsorption enthalpy and thermal Gibbs free energy change are $\Delta H_{ads} = -134.3$ and $\Delta G_{ads} = -56.1$ kJ/mol under room conditions (293.15 K, 101325 Pa), respectively; then, the formation of the complex is an exothermic and spontaneous process. Comparatively, the interaction electronic energy of the complex (without the thermal effects and destabilization coming from nuclear motions) is $\Delta E_{int} = -142.7$ kJ/mol, which is comparable to the adsorption enthalpy change ($\Delta H_{ads} = -134.3$

https://doi.org/10.1021/acsami.3c18038
ACS Appl. Mater. Interfaces XXXX, XXX, XXX−XXX

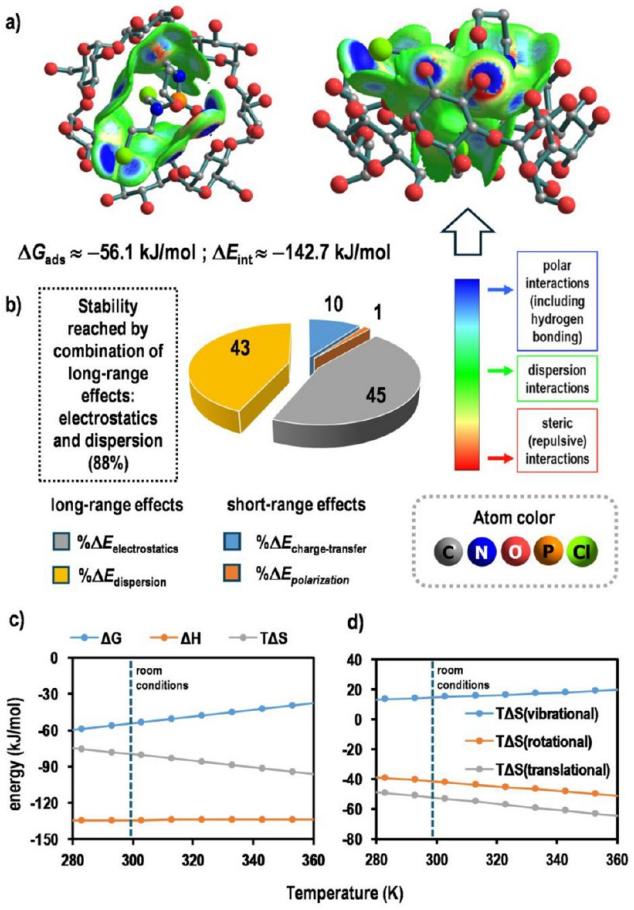

Figure 13. Computed properties of the NSs-CYC complex: Ground state and IGMH analysis of weak interactions (A), energy decomposition analysis of the interaction energy (B), thermodynamic parameters as a function of temperature (C), and vibrational, rotational, and translational terms of the entropy change ($T\Delta S$) as a function of temperature (D).

kJ/mol). Consequently, and considering that $\Delta G_{ads} = \Delta H_{ads} - T\Delta S_{ads}$ (where ΔS_{ads} is the adsorption entropy change), the $T\Delta S_{ads}$ term appears as an unfavorable contribution for the complex formation at room conditions. In other words, the entropy effects raise the energy of the complex but are not high enough to hinder the spontaneous drug loading under room conditions. In this regard, although the ΔS_{ads} term is low, the temperature dependence of $T\Delta S_{ads}$ allows the compensation of the enthalpy change, resulting in that $\Delta H_{ads} < \Delta G_{ads}$. With respect to the interaction mechanism, density-based analysis (isosurfaces in Figure 13A) indicated that dispersion effects (physical entrapment and green isosurfaces) and several pairwise interactions of electrostatic nature, such as CH···Cl, OH···Cl, CH···CH, and hydrogen bonding (blue regions), were the main long-range physical effects determining complex stability. Accordingly, energy decomposition analysis of the interaction energies indicated that dispersion ($\Delta E_{dispersion}$) and Coulombic electrostatic attractions ($\Delta E_{electrostatics}$) contributed to the stabilizing energy, by 43 and 45%, respectively. On the other hand, charge transfer and polarization short-range effects displayed a weak combined contribution (11%), in agreement with the lack of orbital overlapping (Figure 13B). Therefore, the spontaneous formation of the noncovalent inclusion complex at room temperature supports favorable drug loading on the NSs.

The magnetic hyperthermia-based releasing process generated heat in the complex, causing adsorption to decrease with increasing temperature due to the exothermic formation of the noncovalent inclusion complex. Figure 13C displays the thermodynamic parameters as a function of the temperature. As shown, the formation of the inclusion complex was an enthalpy-driven process at room temperature ($\Delta H_{ads} < T\Delta S_{ads}$, where ΔS_{ads} is the entropy change); nevertheless, the spontaneity of the process decreased as the temperature rose due to the increase of the required entropy changes that allow the physisorption process at higher temperatures. When the complex is formed, there is a loss of rotational and translational entropies ($T\Delta S_{rotational}$ and $T\Delta S_{translational}$), which relate to the steric barrier caused by the molecular structure of the host system and translation/rotation restrictions of the guest molecule (Figure 13D). The loss of rotational and translational entropy increases at higher temperatures, resulting in the $T\Delta S_{ads}$ term overcompensating for the enthalpy change, which decreases the spontaneous formation of the complex and exerts long-range effects. Therefore, drug release was an entropy-driven process facilitated by local heat generation via magnetic hyperthermia and proceeded without an extra energy barrier resulting from the noncovalent nature of the inclusion complex.

3.7. MTS and Effects on Mitochondrial Activity. MTS assays were performed to evaluate the impact of the NSs-CYC and MNPs-NSs-CYC complexes on mitochondrial activity. HeLa cells were chosen for this experiment because they are a human cancer cell line. Therefore, the effects of NSs-CYC and MNPs-NSs-CYC on mitochondrial activity were tested and compared at different concentrations. Moreover, free NSs (1:4) and CYC were tested and evaluated as controls, as shown in Figure 14.

The results showed that CYC significantly reduced mitochondrial activity at concentrations above 0.03 mg/mL. However, the developed NSs-CYC complexes did not exert cytotoxicity on the HeLa cells at the concentrations tested, except for the highest concentration of NSs-CYC (0.03 mg/mL). The NSs-CYC complex presented a 3-fold difference in mitochondrial activity compared to free CYC. Furthermore, NSs-CYT showed no significant difference from the medium at any of the evaluated concentrations. The aforementioned results were also independently observed for MNPs-NSs-CYC and NSs. This finding is promising because it indicates that the encapsulation of CYC reduces its toxic effects on HeLa cell lines and that the association of MNPs to the organic matrix does not affect mitochondrial activity while also imparting superparamagnetic properties to the NSs-drug systems.

3.8. Effect of Magnetic Hyperthermia on the Ternary System in the Presence of HeLa Cells. The influence of an AMF on HeLa cells treated with bare MNPs and MNPs-NSs-CYC was investigated as a function of Fe content (0.5 and 1 mg/mL), utilizing a frequency of 734 kHz and a magnetic field intensity of 10 mT. Following 72 h of AMF exposure, fluorescence microscopy analysis (after Hoechst staining) revealed a significant decrease in cell numbers in groups treated with MNPs at 0.5 and 1 mg/mL (40.0 ± 4.5 and 21.2 ± 6.7, respectively) and with MNPs-NSs-CYC at 0.5 and 1 mg/mL (42.4 ± 8.2 and 20.2 ± 2.2, respectively), compared to the control and field control groups (74.4 ± 7.6 and 68.8 ± 4.4, respectively; Figure 15A,B). Notably, the cell counts were similar between the MNPs and MNPs-NSs-CYC systems despite the significant decrease in the heating capacity of MNPs-NSs-CYC, as illustrated in Figure 10. One possible

https://doi.org/10.1021/acsami.3c18038
ACS Appl. Mater. Interfaces XXXX, XXX, XXX−XXX

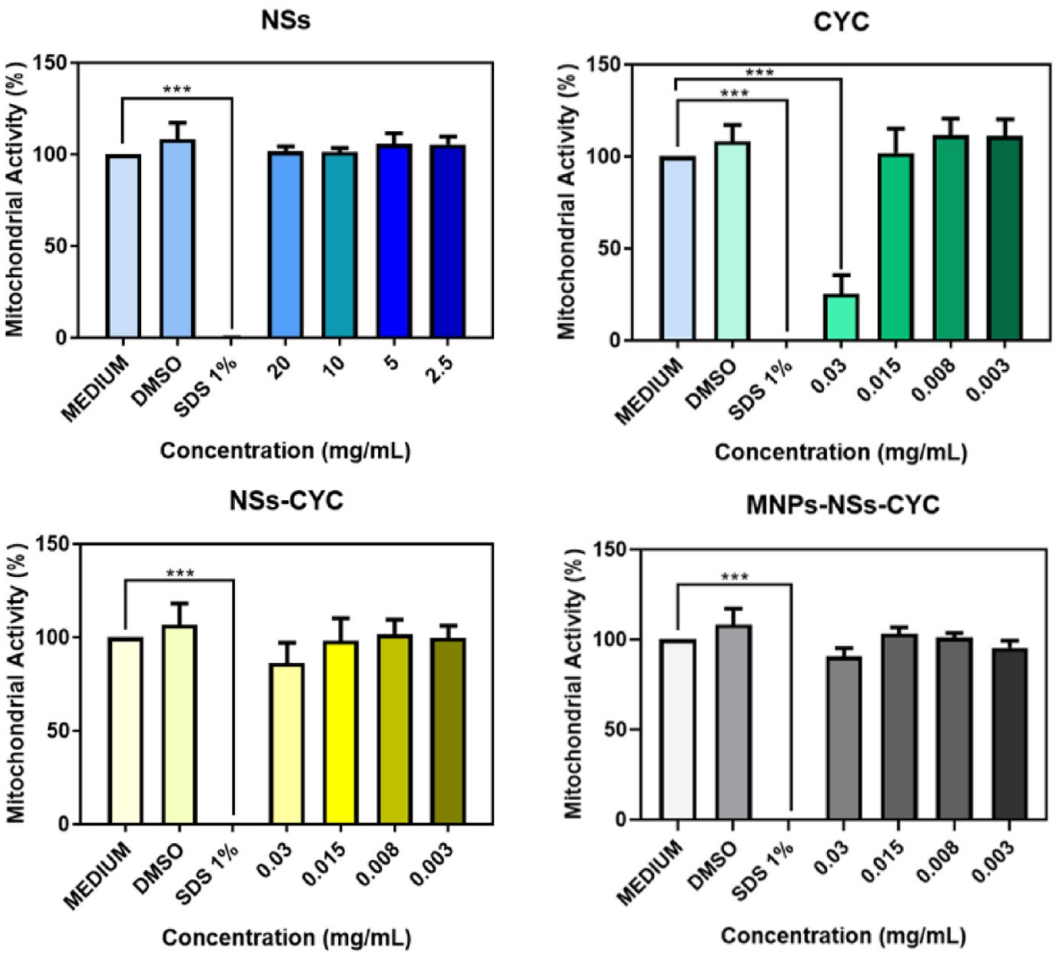

Figure 14. Effects of free NSs, CYC, NSs-CYC, and MNPs-NSs-CYC on mitochondrial activity, determined with an MTS assay. The data are represented as percentages compared with the medium and shown as the mean ± SEM of three independent experiments. The statistical significance is indicated with ***$p < 0.001$. DMSO 1% and SDS 1% were used as positive and negative controls, respectively.

explanation for this phenomenon is that since the cells were treated with the compounds 12 h before to facilitate internalization, it is conceivable that, during that time, NSs underwent degradation, thereby releasing both the embedded MNPs and CYC. Consequently, upon application of the AMF, both MNPs and MNPs-NSs-CYC systems exerted similar effects. Moreover, temperature curve analyses evidenced the same temperature increments in both MNPs (38.2 ± 0.36 and 38.2 ± 0.36 °C) and MNPs-NSs-CYC (38.02 ± 0.15 and 38.14 ± 0.36), supporting the hypothesis of NSs degradation and subsequent MNPs and drug release. Although magnetic hyperthermia treatments aim for temperatures that exceed 40 °C, the observed temperatures were lower due to environmental heat loss during experimentation. More importantly, the treatment with the MNPs-NSs-CYC ternary system and the local hyperthermia induced by the application of AMF allowed reduction of the cell viability of tumor cells. These findings provide initial insights into the behavior of the synthesized ternary compounds under AMF application in in vitro assays. In future experiments, drug release as a function of the concentration of CYC under these conditions and the effects on the viability of cancer cells will be evaluated.

4. CONCLUSIONS

We successfully synthesized an inclusion compound consisting of an NSs-CYC drug system associated with MNPs. As proven by VSM, DLS, ζ-potential, XPS, TEM, SAED, XRPD, FE-SEM, and EDS characterization, the ternary system provides stability to the MNPs, exhibits superparamagnetic behavior, and allows the anticancer drug CYC to be encapsulated. MTS assays were performed to evaluate the effect of the NSs-CYC and MNPs-NSs-CYC complexes on HeLa cells. The results showed that CYC significantly reduced mitochondrial activity at concentrations above 0.03 mg/mL. However, the developed ternary systems proved safer than the free drug, as they did not exert cytotoxicity on the HeLa cells at the assayed concentrations. The magnetic NSs that contained the anticancer drug were able to respond to an external AMF, enabling the controlled release of the drug from the ternary systems, which reached a maximum free drug concentration of 0.023 mg/mL. Thus, the hypothesis that the superparamagnetic ternary system could effectively release CYC through magnetic hyperthermia was validated. These promising results allowed us to visualize potential applications in the controlled release of anticancer agents using a non-invasive strategy such as applying an AMF. Our research contributes to the field by introducing a drug release mechanism utilizing a supramolecular system of NSs through magnetic hyperthermia. This underscores the potential of the

https://doi.org/10.1021/acsami.3c18038
ACS Appl. Mater. Interfaces XXXX, XXX, XXX−XXX

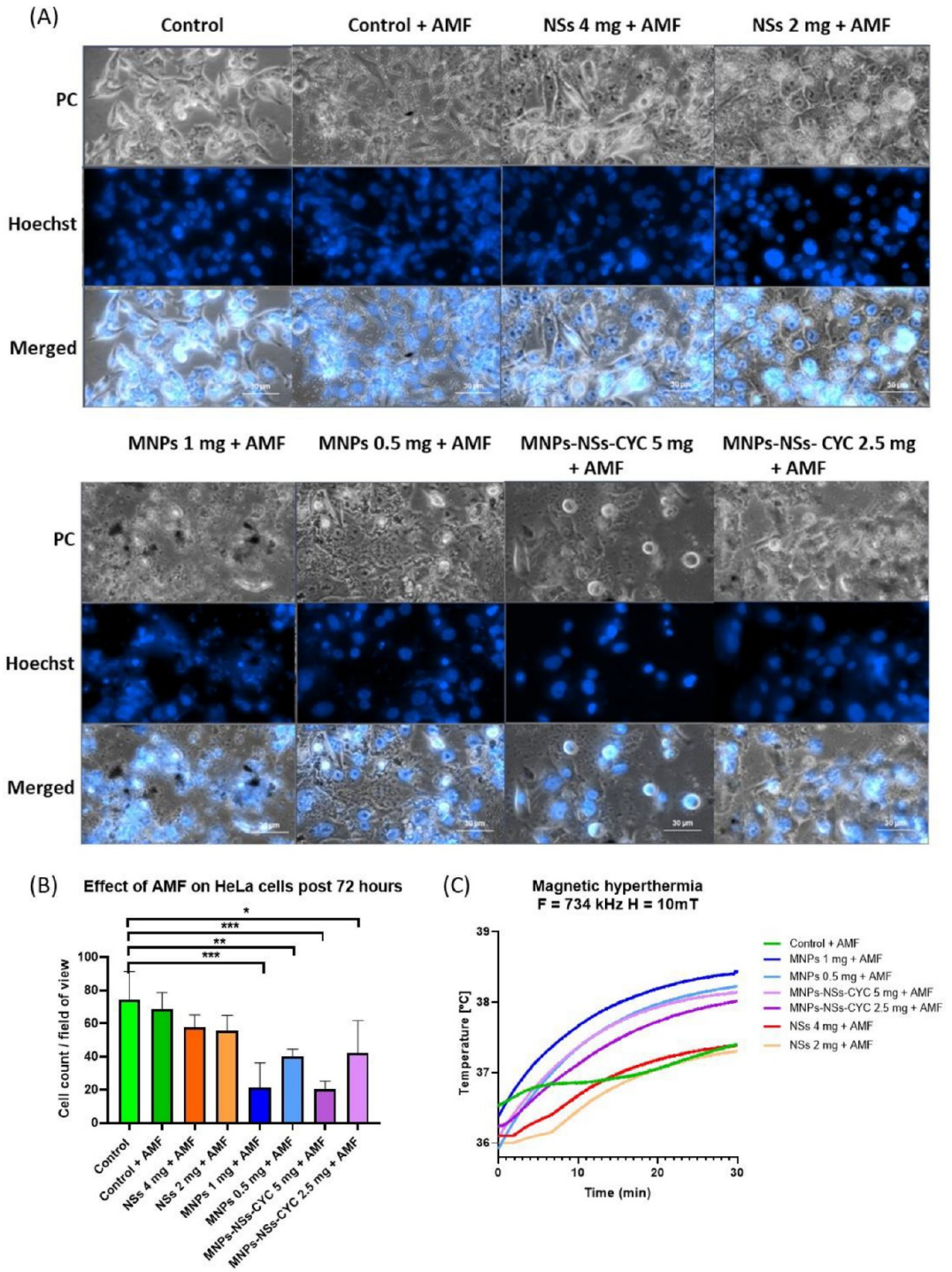

Figure 15. Effect of the application of AMF on HeLa cells treated with NSs, MNPs, and MNPs-NSs-CYC. Fluorescence microscopy analysis (A) revealed a significant decrease in cell numbers in groups treated with MNPs and MNPs-NSs-CYC (B). Temperature increments were observed in the groups treated with MNPs and MNPs-NSs-CYC (C). The data are represented as the mean ± SEM of three independent experiments. The statistical significance is indicated with ***$p < 0.001$.

proposed technology for localized drug delivery systems. However, it is essential to acknowledge limitations such as the need to further optimize the parameters for enhanced drug release efficiency. The applicability of these systems to other anticancer drugs must also be explored. Investigating the encapsulation and release profiles of various drugs will broaden the potential applications of the proposed formulation. The prospects of these systems encompass evaluating the effects of drug release triggered by local hyperthermia on human cancer cell lines to evaluate their viability as efficient, safe, and effective tumor treatments. Future studies should aim to enhance the stimulus-responsive nature of NSs-drug-MNPs ternary systems. Methods for regulating heat generation and refining the ternary system's responsiveness to AMF parameters can further improve drug release precision. Extensive in vitro studies and exploration of combination therapies are also crucial to assessing the

https://doi.org/10.1021/acsami.3c18038
ACS Appl. Mater. Interfaces XXXX, XXX, XXX−XXX

biocompatibility and safety of the NSs-drug-MNPs complexes and the possibility of creating synergistic effects with other therapeutic modalities.

■ ASSOCIATED CONTENT

Data Availability Statement

Data will be available on request.

■ AUTHOR INFORMATION

Corresponding Authors

Sebastián Salazar Sandoval − *Departamento de Química, Facultad de Ciencias, Universidad de Chile, Santiago 7800003, Chile; Departamento de Química Farmacológica y Toxicológica, Universidad de Chile, Santiago 8380492, Chile; Advanced Center for Chronic Diseases (ACCDiS), Universidad de Chile, Santiago 8380494, Chile; Facultad de Diseño, Universidad del Desarrollo, Santiago 7610658, Chile*; Email: sebastian.salazar@udd.cl

Marcelo J. Kogan − *Departamento de Química Farmacológica y Toxicológica, Universidad de Chile, Santiago 8380492, Chile; Advanced Center for Chronic Diseases (ACCDiS), Universidad de Chile, Santiago 8380494, Chile*; Email: mkogan@ciq.uchile.cl

Paul Jara − *Departamento de Química, Facultad de Ciencias, Universidad de Chile, Santiago 7800003, Chile*; orcid.org/0000-0002-0575-2135; Email: pjara@uchile.cl

Authors

Patricia Díaz-Saldívar − *Laboratorio de Nanomedicina y Biosensores, Center for the Development of Nanoscience and Nanotechnology (CEDENNA), Universidad de Santiago de Chile (USACH), Santiago 9170022, Chile*

Ingrid Araya − *Departamento de Ciencias Básicas, Facultad de Ciencias, Universidad Santo Tomás, Santiago 8370003, Chile*

Freddy Celis − *Laboratorio de Procesos Fotónicos y Electroquímicos, Facultad de Ciencias Naturales y Exactas, Universidad de Playa Ancha, Valparaíso 2360002, Chile*; orcid.org/0000-0003-3195-3018

Diego Cortés-Arriagada − *Instituto Universitario de Investigación y Desarrollo Tecnológico, Universidad Tecnológica Metropolitana, Santiago 8940577, Chile*; orcid.org/0000-0002-6709-1723

Ana Riveros − *Departamento de Química Farmacológica y Toxicológica, Universidad de Chile, Santiago 8380492, Chile; Advanced Center for Chronic Diseases (ACCDiS), Universidad de Chile, Santiago 8380494, Chile*

Carlos Rojas-Romo − *Departamento de Química, Facultad de Ciencias, Universidad de Chile, Santiago 7800003, Chile*

⬢**Carolina Jullian** − *Departamento de Química Orgánica y Fisicoquímica, Universidad de Chile, Santiago 8380492, Chile*; orcid.org/0000-0001-6902-7170

Nataly Silva − *Facultad de Diseño, Universidad del Desarrollo, Santiago 7610658, Chile*

Nicolás Yutronic − *Departamento de Química, Facultad de Ciencias, Universidad de Chile, Santiago 7800003, Chile*

Complete contact information is available at: https://pubs.acs.org/10.1021/acsami.3c18038

Author Contributions

¶S.S.S. and P.D.-S. contributed equally to this work.

Notes

The authors declare no competing financial interest.

⬢Deceased November 20, 2022.

■ ACKNOWLEDGMENTS

We acknowledge the Postdoctoral Research Project UDD 2024 (Sebastián Salazar Sandoval), the FONDEQUIP projects EQM 170111 and EQM 180180; the FONDAP projects 15130011 and Apoyo 1523A0008; Anillo ACT 210068; BASAL Project AFB220001, CEDENNA; FONDECYT projects 1200782 and 1210355; and Proyecto Enlace ENL 01/22 VID (Paul Jara), Universidad de Chile.

■ DEDICATION

Dedicated to the memory of José Salazar and Claudio Sandoval.

■ REFERENCES

(1) Dong, P.; Rakesh, K.; Manukumar, H.; Mohammed, Y.; Karthik, C.; Sumathi, S.; Mallu, P.; Qin, H. Innovative Nano-carriers in Anticancer Drug Delivery-a Comprehensive Review. *Bioorg. Chem.* **2019**, *85*, 325−336.

(2) Moradi Kashkooli, F.; Soltani, M.; Souri, M. Controlled Anti-cancer Drug Release through Advanced Nano-drug Delivery Systems: Static and Dynamic Targeting Strategies. *J. Controlled Release* **2020**, *327*, 316−349.

(3) Voelcker, G. The Mechanism of Action of Cyclophosphamide and its Consequences for the Development of a New Generation of Oxazaphosphorine Cytostatics. *Sci. Pharm.* **2020**, *88*, 42.

(4) Gholibegloo, E.; Mortezazadeh, T.; Salehian, F.; Forootanfar, H.; Firoozpour, L.; Foroumadi, A.; Ramazani, A.; Khoobi, M. Folic Acid Decorated Magnetic Nanosponge: An Efficient Nanosystem for Targeted Curcumin Delivery and Magnetic Resonance Imaging. *J. Colloid Interface Sci.* **2019**, *556*, 128−139.

(5) Poulson, B. G.; Alsulami, Q. A.; Sharfalddin, A.; El Agammy, E. F.; Mouffouk, F.; Emwas, A.-H.; Jaremko, L.; Jaremko, M. Cyclodextrins: Structural, Chemical, and Physical Properties, and Applications. *Polysaccharides* **2022**, *3*, 1−31.

(6) Munir, R.; Hadi, A.; Khan, S.; Asghar, S.; Irfan, M.; Khan, I.; Hameed, M.; Inam, S.; Islam, N.; Hassan, S.; et al. Solubility and Dissolution Enhancement of Dexibuprofen with Hydroxypropylbeta-cyclodextrin (HPβCD) and Poloxamers (188/407) Inclusion Complexes: Preparation and In Vitro Characterization. *Polymers (Basel)* **2022**, *14*, 579.

(7) Mohammed-Saeid, W.; Karoyo, A. H.; Verrall, R. E.; Wilson, L. D.; Badea, I. Inclusion Complexes of Melphalan with Gemini-conjugated β-cyclodextrin: Physicochemical Properties and Chemotherapeutic Efficacy in In-vitro Tumor Models. *Pharmaceutics* **2019**, *11*, 427.

(8) Adeoye, O.; Bartolo, I.; Conceicao, J.; Da Silva, A.; Duarte, N.; Francisco, A.; Taveira, N.; Cabral-Marques, H. Pyromellitic Dianhydride Crosslinked Soluble Cyclodextrin Polymers: Synthesis, Lopinavir Release from Sub-micron Sized Particles and Anti-HIV-1 Activity. *Int. J. Pharm.* **2020**, *583*, No. 119356.

(9) Moin, A.; Roohi, N. K. F.; Rizvi, S. M. D.; Ashraf, S. A.; Siddiqui, A. J.; Patel, M.; Ahmed, S. M.; Gowda, D. V.; Adnan, M. Design and Formulation of Polymeric Nanosponge Tablets with Enhanced Solubility for Combination Therapy. *RSC Adv.* **2020**, *10*, 34869−34884.

(10) Real, D. A.; Bolaños, K.; Priotti, J.; Yutronic, N.; Kogan, M. J.; Sierpe, R.; Donoso-González, O. Cyclodextrin-modified Nanomaterials for Drug Delivery: Classification and Advances in Controlled Release and Bioavailability. *Pharmaceutics* **2021**, *13*, 2131.

(11) Krabicova, I.; Appleton, S. L.; Tannous, M.; Hoti, G.; Caldera, F.; Rubin Pedrazzo, A.; Cecone, C.; Cavalli, R.; Trotta, F. History of Cyclodextrin Nanosponges. *Polymers (Basel)* **2020**, *12*, 1122.

(12) Deng, J.; Chen, Q.; Li, W.; Zuberi, Z.; Feng, J.; Lin, Q.; Ren, J.; Luo, F.; Ding, Q.; Zeng, X.; Ma, L.; Yin, H.; Zheng, X. Toward Improvements for Carrying Capacity of the Cyclodextrin-based Nanosponges: Recent Progress from a Material and Drug Delivery. *J. Mater. Sci.* **2021**, *56*, 5995−6015.

https://doi.org/10.1021/acsami.3c18038
ACS Appl. Mater. Interfaces XXXX, XXX, XXX−XXX

(13) Tiwari, P.; Vig, K.; Dennis, V.; Singh, S. Functionalized Gold Nanoparticles and Their Biomedical Applications. *Nanomaterials* **2011**, *1*, 31−63.
(14) Jara-Guajardo, P.; Cabrera, P.; Celis, F.; Soler, M.; Berlanga, I.; Parra-Munoz, N.; Acosta, G.; Albericio, F.; Guzman, F.; Campos, M.; Alvarez, A.; Morales-Zavala, F.; Kogan, M. J Gold Nanoparticles Mediate Improved Detection of β-amyloid Aggregates by Fluorescence. *Nanomaterials* **2020**, *10*, 690.
(15) Ishtiaq, S.; Shah, K. U.; Ur-Rehman, T.; Ud-Din, F. Gold Nanorods: New Generation Drug Delivery Platform. *Met. Nanopart. Drug Delivery Diagn. Appl.* **2020**, 59−84.
(16) Starón, A.; Dlugosz, O.; Pulit-Prociak, J.; Banach, M. Analysis of the Exposure of Organisms to the Action of Nanomaterials. *Materials* **2020**, *13*, 349.
(17) Ali, M. R. K.; Wu, Y.; El-Sayed, M. A. Gold-Nanoparticle-Assisted Plasmonic Photothermal Therapy Advances Toward Clinical Application. *J. Phys. Chem. C* **2019**, *123*, 15375−15393.
(18) Rudhrabatla, V. S. A. P.; Sudhakar, B.; Reddy, K. V. N. S. In Vitro and In Vivo Assessment of Designed Melphalan Loaded Stealth Solid Lipid Nanoparticles for Parenteral Delivery. *J. Bionanosci.* **2020**, *10*, 168−190.
(19) Zhao, J.; Zhong, D.; Zhou, S. NIR-I-to-NIR-II Fluorescent Nanomaterials for Biomedical Imaging and Cancer Therapy. *J. Mater. Chem. B* **2018**, *6*, 349−365.
(20) Allahyari, S.; Zahednezhad, F.; Khatami, M.; Hashemzadeh, N.; Zakeri-Milani, P.; Trotta, F. Cyclodextrin Nanosponges as Potential Anticancer Drug Delivery Systems to be Introduced into the Market, Compared with Liposomes. *J. Drug Delivery Sci. Technol.* **2022**, *67*, No. 102931.
(21) Salazar, S.; Yutronic, N.; Kogan, M. J.; Jara, P. Cyclodextrin Nanosponges Inclusion Compounds Associated with Gold Nanoparticles for Potential Application in the Photothermal Release of Melphalan and Cytoxan. *Int. J. Mol. Sci.* **2021**, *22*, 6446.
(22) Salazar Sandoval, S.; Cortés-Adasme, E.; Gallardo-Toledo, E.; Araya, I.; Celis, F.; Yutronic, N.; Jara, P.; Kogan, M. J. β-Cyclodextrin-Based Nanosponges Inclusion Compounds Associated with Gold Nanorods for Potential NIR-II Drug Delivery. *Pharmaceutics* **2022**, *14*, 2206.
(23) Omorogbe, S. O.; Aigbodion, A.; Ifijen, H.; Simo, A.; Obgeide-Ihama, N.; Ikhuoria, E. Low-Temperature Synthesis of Superparamagnetic Fe3O4 Morphologies Tuned Using Oleic Acid as Crystal Growth Modifiers. In *TMS 2020 149th Annual Meeting & Exhibition Supplemental Proceedings*; The Minerals, Metals & Materials Series; Springer, 2020. DOI: 10.1007/978-3-030-36296-6_58
(24) Salazar, S.; Yutronic, N.; Jara, P. Magnetic β-Cyclodextrin Nanosponges for Potential Application in the Removal of the Neonicotinoid Dinotefuran from Wastewater. *Int. J. Mol. Sci.* **2020**, *21*, 4079.
(25) Caldera, F.; Nistico, R.; Magnacca, G.; Matencio, A.; Khazaei Monfared, Y.; Trotta, F. Magnetic Composites of Dextrin-Based Carbonate Nanosponges and Iron Oxide Nanoparticles with Potential Application in Targeted Drug Delivery. *Nanomaterials* **2022**, *12*, 754.
(26) Salazar, S.; Guerra, D.; Yutronic, N.; Jara, P. Removal of aromatic chlorinated pesticides from aqueous solution using β-cyclodextrin polymers decorated with Fe3O4 nanoparticles. *Polymers (Basel)* **2018**, *10*, 1038.
(27) Jędrzak, A.; Grzeskowiak, B.; Golba, K.; Coy, E.; Synoradzki, K.; Jurga, S.; Jesionowski, T.; Mrowczynski, R. Magnetite Nanoparticles and Spheres for Chemo-and Photothermal Therapy of Hepatocellular Carcinoma in Vitro. *Int. J. Nanomed.* **2020**, *15*, 7923−7936.
(28) Sengupta, S.; Balla, V. K. A Review on the Use of Magnetic Fields and Ultrasound for Non-Invasive Cancer Treatment. *J. Adv. Res.* **2018**, *14*, 97−111.
(29) Mohammadi, M.; Pourseyed Aghaei, F. Magnetite Fe3O4 Surface as an Effective Drug Delivery System for Cancer Treatment Drugs: Density Functional Theory Study. *J. Biomol. Struct. Dyn.* **2021**, *39*, 2798−2805.
(30) Wu, K.; Su, D.; Liu, J.; Saha, R.; Wang, J. P. Magnetic Nanoparticles in Nanomedicine: A Review of Recent Advances. *Nanotechnology* **2019**, *30*, 502003.
(31) Yamaminami, T.; Ota, S.; Trisnanto, S.; Ishikawa, M.; Yamada, T.; Yoshida, T.; Enpuku, K.; Takemura, Y. Power Dissipation in Magnetic Nanoparticles Evaluated Using the AC Susceptibility of their Linear and Nonlinear Responses. *J. Magn. Mater.* **2021**, *517*, No. 167401.
(32) Alfareed, T. M.; Slimani, Y.; Almessiere, M.; Shirsath, S.; Hassan, M.; Nawaz, M.; Khan, F.; Al-Suhaimi, E.; Baykal, A. Structure, Magnetoelectric, and Anticancer Activities of Core-Shell Co0·8Mn0.2R0.02Fe1·98O4@BaTiO3 Nanocomposites (R = Ce, Eu, Tb, Tm, or Gd). *Ceram. Int.* **2022**, *48*, 14640−14651.
(33) Almessiere, M.A.; Slimani, Y.; Rehman, S.; Khan, F. A.; Polat, E. G.; Sadaqat, A.; Shirsath, S. E.; Baykal, A. Synthesis of Dy-Y Co-Substituted Manganese-Zinc Spinel Nanoferrites Induced Antibacterial and Anti-cancer Activities: Comparison Between Sonochemical and Sol-gel Auto-Combustion Methods. *Mater. Sci. Eng.: C* **2020**, *116*, 111186.
(34) Kouzoudis, D.; Samourgkanidis, G.; Kolokithas-Ntoukas, A.; Zoppellaro, G.; Spiliotopoulos, K. Magnetic Hyperthermia in the 400−1,100 kHz Frequency Range Using MIONs of Condensed Colloidal Nanocrystal Clusters. *Front. Mater.* **2021**, *8*, 638019.
(35) Khan, A. S.; Nasir, M. F.; Khan, M. T.; Murtaza, A.; Hamayun, M. A. Study of Structural, Magnetic and Radio Frequency Heating Aptitudes of Pure and (Fe-III) Doped Manganite (La1-x SrxMnO3) and Their Incorporation with Sodium Poly-Styrene Sulfonate (PSS) for Magnetic Hyperthermia Applications. *Physica. B. Condens. Mater.* **2021**, *600*, No. 412627.
(36) Attaluri, A.; Kandala, S.; Zhou, H.; Wabler, M.; DeWeese, T.; Ivkov, R. Magnetic Nanoparticle Hyperthermia for Treating Locally Advanced Unresectable and Borderline Resectable Pancreatic Cancers: the Role of Tumor Size and Eddy-Current Heating. *Int. J. Hyperthermia* **2020**, *37*, 108−119.
(37) Almessiere, M. A.; Slimani, Y.; Rehman, S.; Khan, F.; Gungunes, C. D.; Guner, S.; Shirsath, S.; Baykal, A. Magnetic Properties, Anticancer and Antibacterial Effectiveness of Sonochemically Produced Ce3+/Dy3+ Co-activated Mn-Zn Nanospinel Ferrites. *Arabian J. Chem.* **2020**, *13*, 7403−7417.
(38) Cruz, M. M.; Ferreira, L.; Alves, A.; Mendo, S.; Ferreira, P.; Godinho, M.; Carvalho, M. Nanoparticles for Magnetic Hyperthermia Chapter Outline. *Nanostruct. Cancer Ther.* **2017**, 485−511.
(39) Tefft, B. J.; Uthamaraj, S.; Harburn, J.; Klabusay, M.; Dragomir-Daescu, D.; Sandhu, G. Cell Labeling and Targeting with Superparamagnetic Iron Oxide Nanoparticles. *J. Visualized Exp.* **2015**, *105*, e53099.
(40) Rajan, A.; Sharma, M.; Sahu, N. K. Assessing Magnetic and Inductive Thermal Properties of Various Surfactants Functionalized Fe3O4 Nanoparticles for Hyperthermia. *Sci. Rep.* **2020**, *10*, 15045.
(41) Nedyalkova, M.; Donkova, B.; Romanova, J.; Tzvetkov, G.; Madurga, S.; Simeonov, V. Iron Oxide Nanoparticles − In vivo/in vitro Biomedical Applications and in Silico Studies. *Adv. Colloid Interface Sci.* **2017**, *249*, 192−212.
(42) Abenojar, E. C.; Wickramasinghe, S.; Bas-Concepcion, J.; Samia, A. C. S. Structural Effects on the Magnetic Hyperthermia Properties of Iron Oxide Nanoparticles. *Prog. Nat. Sci: Mater. Int.* **2016**, *26*, 440−448.
(43) Espinosa, A.; Bugnet, M.; Radtke, G.; Neveu, S.; Botton, G.; Wilhelm, C.; Abou-Hassan, A. Can Magneto-Plasmonic Nanohybrids Efficiently Combine Photothermia with Magnetic Hyperthermia? *Nanoscale* **2015**, *7*, 18872−18877.
(44) Ahn, T.; Kim, J. H.; Yang, H. M.; Lee, J. W.; Kim, J. D. Formation Pathways of Magnetite Nanoparticles by Coprecipitation Method. *J. Phys. Chem. C* **2012**, *116*, 6069−6076.
(45) Kumar, S.; Pooja; Trotta, F.; Rao, R. Encapsulation of Babchi Oil in Cyclodextrin-Based Nanosponges: Physicochemical Characterization, Photodegradation, and in Vitro Cytotoxicity Studies. *Pharmaceutics* **2018**, *10*, 169.
(46) Salawi, A.; Alam, M.; Zaman, M.; Qureshi, S.; Shah, S.; Majeed, I.; Farooq, U.; Mustafa, W.; Shamim, Q.; Siddique, W.; Almoshari, Y.;

https://doi.org/10.1021/acsami.3c18038
ACS Appl. Mater. Interfaces XXXX, XXX, XXX−XXX

Alshamrani, M. Optimization and Fabrication of the Nanosponge Carriers of on Dansetron Using One-Factor Design. *Pak. J. Pharm. Sci.* **2022**, *35*, 1135−1142.
(47) Pawar, S.; Shende, P.; Trotta, F. Diversity of β-Cyclodextrin-Based Nanosponges for Transformation of Actives. *Int. J. Pharm.* **2019**, *565*, 333−350.
(48) Garrido, B.; González, S.; Hermosilla, J.; Millao, S.; Quilaqueo, M.; Guineo, J.; Acevedo, F.; Pesenti, H.; Rolleri, A.; Shene, C.; Rubilar, M. Carbonate-β-Cyclodextrin-Based Nanosponge as a Nanoencapsulation System for Piperine: Physicochemical Characterization. *J. Soil Sci. Plant Nutr.* **2019**, *19*, 620−630.
(49) Rezaei, A.; Khavari, S.; Sami, M. Incorporation of Thyme Essential Oil into the β-Cyclodextrin Nanosponges: Preparation, Characterization and Antibacterial Activity. *J. Mol. Struct.* **2021**, *1241*, No. 130610.
(50) Lemine, O. M.; Algessair, S.; Madkhali, N.; Al-Najar, B.; El-Boubbou, K. Assessing the Heat Generation and Self-Heating Mechanism of Superparamagnetic Fe3O4 Nanoparticles for Magnetic Hyperthermia Application: The Effects of Concentration, Frequency, and Magnetic Field. *Nanomaterials* **2023**, *13*, 453.
(51) Marenich, A. V.; Cramer, C. J.; Truhlar, D. G. Universal Solvation Model Based on Solute Electron Density and on a Continuum Model of the Solvent Defined by the Bulk Dielectric Constant and Atomic Surface Tensions. *J. Phys. Chem. B* **2009**, *113*, 6378−6396.
(52) Mao, Y.; Loipersberger, M.; Kron, K.; Derrick, J.; Chang, C.; Sharada, S.; Head-Gordon, M. Consistent Inclusion of Continuum Solvation in Energy Decomposition Analysis: Theory and Application to Molecular CO2 Reduction Catalysts. *Chem. Sci.* **2021**, *12*, 1398−1414.
(53) Shringirishi, M.; Mahor, A.; Gupta, R.; Prajapati, S.; Bansal, K.; Kesharwani, P. Fabrication and Characterization of Nifedipine Loaded β-Cyclodextrin Nanosponges: An in Vitro and in Vivo Evaluation. *J. Drug Delivery Sci. Technol.* **2017**, *41*, 344−350.
(54) Pushpalatha, R.; Selvamuthukumar, S.; Kilimozhi, D. Cyclodextrin Nanosponge Based Hydrogel for the Transdermal Co-delivery of Curcumin and Resveratrol: Development, Optimization, In Vitro and Ex Vivo Evaluation. *J. Drug Delivery Sci. Technol.* **2019**, *52*, 55−64.
(55) Varan, C.; Anceschi, A.; Sevli, S.; Bruni, N.; Giraudo, L.; Bilgic, E.; Korkusuz, P.; Iskit, A.; Trotta, F.; Bilensoy, E. Preparation and Characterization of Cyclodextrin Nanosponges for Organic Toxic Molecule Removal. *Int. J. Pharm.* **2020**, *585*, 119485.
(56) Munjal, B.; Zode, S. S.; Bansal, A. K. Crystallization of Cyclophosphamide Monohydrate During Lyophilization. *J. Pharm. Sci.* **2019**, *108*, 1195−1202.
(57) Rizvi, S. S. B.; Akhtar, N.; Minhas, M. U.; Mahmood, A.; Khan, K. U. Synthesis and Characterization of Carboxymethyl Chitosan Nanosponges with Cyclodextrin Blends for Drug Solubility Improvement. *Gels* **2022**, *8*, 55.
(58) Zafar, N.; Mahmood, A.; Sarfraz, R.; Ijaz, H.; Ashraf, M.; Mehr, S. Facile Synthesis of β-Cyclodextrin-Cyclophosphamide Complex-Loaded Hydrogel for Controlled Release Drug Delivery. *Polym. Bull.* **2023**, *80*, 10939−10971.
(59) Mohammed, L.; Gomaa, H. G.; Ragab, D.; Zhu, J. Magnetic Nanoparticles for Environmental and Biomedical Applications: A Review. *Particuology* **2017**, *30*, 1−14.
(60) Farcas, C. G.; Macasoi, I.; Pinzaru, I.; Chirita, M.; Chirita Mihaila, M. C.; Dehelean, C.; Avram, S.; Loghin, F.; Mocanu, L.; Rotaru, V.; Ieta, A.; Ercuta, A.; Coricovac, D. Controlled Synthesis and Characterization of Micrometric Single Crystalline Magnetite With Superparamagnetic Behavior and Cytocompatibility/Cytotoxicity Assessments. *Front. Pharmacol.* **2020**, *11*, 410.
(61) Antal, I.; Koneracka, M.; Kubovcikova, M.; Zavisova, V.; Khmara, I.; Lucanska, D.; Jelenska, L.; Vidlickova, I.; Zatovicova, M.; Pastorekova, S.; Bugarova, N.; Micusik, M.; Omastova, M.; Kopcansky, P. D,L-lysine Functionalized Fe3O4 Nanoparticles for Detection of Cancer Cells. *Colloids Surf., B* **2018**, *163*, 236−245.
(62) Haghgoo, A. A.; Cheraghi, M.; Sobhanardakani, S.; Lorestani, B.; Izadkhah, V. Preparation Of AC/KOH and AC/Fe3O4/ZnO Nanocomposite From Waste Rice Straw for the Removal Of Cyclophosphamide from Aqueous Solutions. *Toxin Rev.* **2023**, *42*, 275−284.
(63) Tanasa, E.; Zaharia, C.; Radu, I.; Surdu, V.; Vasile, B.; Damian, C.; Andronescu, E. Novel Nanocomposites Based on Functionalized Magnetic Nanoparticles and Polyacrylamide: Preparation and Complex Characterization. *Nanomaterials* **2019**, *9*, 1384.
(64) Atrei, A.; Lesiak-Orlowska, B.; Tóth, J. Magnetite Nanoparticles Functionalized with Citrate: A Surface Science Study by XPS and ToF-SIMS. *Appl. Surf. Sci.* **2022**, *602*, 154366.
(65) Upadhyay, S.; Parekh, K.; Pandey, B. Influence of Crystallite Size on the Magnetic Properties of Fe3O4 Nanoparticles. *J. Alloys Compd.* **2016**, *678*, 478−485.
(66) Zandipak, R.; Sobhan Ardakani, S.; Shirzadi, A. Synthesis and Application of Nanocomposite Fe3O4@SiO2@CTAB−SiO2 as a Novel Adsorbent for Removal of Cyclophosphamide from Water Samples. *Sep. Sci. Technol. (Philadelphia, P.A., U.S.)* **2020**, *55*, 456−470.
(67) Khalil, M. I. Co-Precipitation in Aqueous Solution Synthesis of Magnetite Nanoparticles Using Iron(III) Salts as Precursors. *Arab. J. Chem.* **2015**, *8*, 279−284.
(68) Wang, R.; Degirmenci, V.; Xin, H.; Li, Y.; Wang, L.; Chen, J.; Hu, X.; Zhang, D. PEI-Coated Fe3O4 Nanoparticles Enable Efficient Delivery of Therapeutic siRNA Targeting REST into Glioblastoma Cells. *Int. J. Mol. Sci.* **2018**, *19*, 2230.
(69) Danaei, M.; Dehghankhold, M.; Ataei, S.; Hasanzadeh Davarani, F.; Javanmard, R.; Dokhani, A.; Khorasani, S.; Mozafari, M. Impact of Particle Size and Polydispersity Index on the Clinical Applications of Lipidic Nanocarrier Systems. *Pharmaceutics* **2018**, *10*, 57.
(70) Włodarczyk, A.; Gorgoń, S.; Radoń, A.; Bajdak-Rusinek, K. Magnetite Nanoparticles in Magnetic Hyperthermia and Cancer Therapies: Challenges and Perspectives. *Nanomaterials* **2022**, *12*, 1807.
(71) Shirvalilou, S.; Khoei, S.; Esfahani, A. J.; Kamali, M.; Shirvaliloo, M.; Sheervalilou, R.; Mirzaghavami, P. Magnetic Hyperthermia as an Adjuvant Cancer Therapy in Combination with Radiotherapy Versus Radiotherapy Alone for Recurrent/Progressive Glioblastoma: a Systematic Review. *J. Neurooncol.* **2021**, *152*, 419−428.
(72) Herrero de la Parte, B.; Rodrigo, I.; Gutierrez-Basoa, J.; Iturrizaga Correcher, S.; Mar Medina, C.; Echevarria-Uraga, J. J.; Garcia, J. A.; Plazaola, F.; Garcia-Alonso, I. Proposal of New Safety Limits for In Vivo Experiments of Magnetic Hyperthermia Antitumor Therapy. *Cancers (Basel)* **2022**, *14*, 3084.
(73) Tsiapla, A. R.; Kalimeri, A.; Maniotis, N.; Myrovali, E.; Samaras, T.; Angelakeris, M.; Kalogirou, O. Mitigation of Magnetic Particle Hyperthermia Side Effects by Magnetic Field Controls. *Int. J. Hyperthermia* **2021**, *38*, 511−522.
(74) Liu, N.N.; Pyatakov, A.P.; Saletsky, A.M.; Zharkov, M.N.; Pyataev, N.A.; Sukhorukov, G.B.; Gun'ko, Y.K.; Tishin, A.M. The "Field or Frequency" Dilemma in Magnetic Hyperthermia: The Case of Zn−Mn Ferrite Nanoparticles. *J. Magn Magn Mater.* **2022**, *555*, No. 169379.
(75) Argenziano, M.; Haimhoffer, A.; Bastiancich, C.; Jicsinszky, L.; Caldera, F.; Trotta, F.; Scutera, S.; Alotto, D.; Fumagalli, M.; Musso, T.; Castagnoli, C.; Cavalli, R. In Vitro Enhanced Skin Permeation and Retention of Imiquimod Loaded in β-Cyclodextrin Nanosponge Hydrogel. *Pharmaceutics* **2019**, *11*, 138.
(76) Pivato, R. V.; Rossi, F.; Ferro, M.; Castiglione, F.; Trotta, F.; Mele, A. β-Cyclodextrin Nanosponge Hydrogels as Drug Delivery Nanoarchitectonics for Multistep Drug Release Kinetics. *ACS Appl. Polym. Mater.* **2021**, *3*, 6562−6571.

https://doi.org/10.1021/acsami.3c18038
ACS Appl. Mater. Interfaces XXXX, XXX, XXX−XXX